REPORT DOCUMENTATION PAGE		READ INSTRUCTIONS BEFORE COMPLETING FORM
1. REPORT NUMBER RPI Math. Rep. No. 144	2. GOVT ACCESSION NO.	3. RECIPIENT'S CATALOG NUMBER
4. TITLE *(and Subtitle)* Current and current shear effects in the parabolic approximation for underwater sound channels		5. TYPE OF REPORT & PERIOD COVERED
		6. PERFORMING ORG. REPORT NUMBER
7. AUTHOR(*s*) W. L. Siegmann, M. J. Jacobson, and J. S. Robertson		8. CONTRACT OR GRANT NUMBER(*s*) N00014-76-C-0288
9. PERFORMING ORGANIZATION NAME AND ADDRESS Rensselaer Polytechnic Institute Troy, New York 12181		10. PROGRAM ELEMENT, PROJECT, TASK AREA & WORK UNIT NUMBERS NR 386-606
11. CONTROLLING OFFICE NAME AND ADDRESS Office of Naval Research, Code 425 Department of the Navy Arlington, Virginia 22217		12. REPORT DATE 30 September 1984
		13. NUMBER OF PAGES 49
14. MONITORING AGENCY NAME & ADDRESS(*if different from Controlling Office*)		15. SECURITY CLASS. *(of this report)*
		15a. DECLASSIFICATION/DOWNGRADING SCHEDULE
16. DISTRIBUTION STATEMENT *(of this Report)* This document has been approved for public release and sale; its distribution is unlimited.		
17. DISTRIBUTION STATEMENT *(of the abstract entered in Block 20, if different from Report)*		
18. SUPPLEMENTARY NOTES		
19. KEY WORDS *(Continue on reverse side if necessary and identify by block number)* Underwater Sound Propagation Current Shear Parabolic Approximations Reciprocal Transmissions Ocean Currents		

20. ABSTRACT *(Continue on reverse side if necessary and identify by block number)*

The effect of currents on the acoustic pressure field in an under-water sound channel is investigated. Based on fundamental fluid equations, model equations are formulated for sound pressure while including nonuniform currents in the source-receiver plane. Application of parabolic-type approximations yields a collection of parabolic equations. Each of these is valid in a different

(continued on back)

DD FORM 1473 EDITION OF 1 NOV 65 IS OBSOLETE
1 JAN 73
S/N 0102-LF-014-6601

domain determined by the magnitudes of current speed, current shear, and depth variation of sound speed. Under certain conditions, it is possible to interpret current effects in terms of an effective sound speed. Using this effective sound speed in an existing numerical code, we examine sound speed in a shallow water isospeed channel with a simple shear flow and a lossy bottom. It is found that even small currents can induce very substantial variations in relative intensity. The degree of variation depends upon current speed, source and receiver geometry, and acoustic frequency. Particular emphasis is placed on intensity-difference predictions in reciprocal sound transmissions in the presence of an ocean current.

Current and Current Shear Effects
in the Parabolic Approximation
for Underwater Sound Channels

by

W. L. Siegmann, M. J. Jacobson
and J. S. Robertson

Department of Mathematical Sciences

Rensselaer Polytechnic Institute |
)\

Troy, New York 12181

RPI Math. Rep. No. 144

September 30, 1984

ABSTRACT

The effect of currents on the acoustic pressure field in an underwater
sound channel is investigated. Based on fundamental fluid equations,
model equations are formulated for sound pressure while including nonuniform
currents in the source-receiver plane. Application of parabolic-type
approximations yields a collection of parabolic equations. Each of these
is valid in a different domain determined by the magnitudes of current
speed, current shear, and depth variation of sound speed. Under certain
conditions, it is possible to interpret current effects in terms of an
effective sound speed. Using this effective sound speed in an existing
numerical code, we examine sound speed in a shallow water isospeed channel
with a simple shear flow and a lossy bottom. It is found that even small
currents can induce very substantial variations in relative intensity.
The degree of variation depends upon current speed, source and receiver
geometry, and acoustic frequency. Particular emphasis is placed on intensity-
difference predictions in reciprocal sound transmissions in the presence of
an ocean current.

INTRODUCTION

Ocean currents have been shown to have both interesting and important effects in underwater sound channels. Major acoustical experiments have emphasized the role of currents, as indicated by a recent review.[1] For instance, it has been suggested[2] that tidal currents may account for certain experimentally measured fluctuations in several shallow and deep water studies. Substantial experimental effort continues at present, in both deep and shallow regions (e.g., Ref.3). Within the context of ray theory, a number of investigations, (e.g., Refs.4-7) have presented comprehensive analyses of some current effects by treating cases of uniform as well as nonuniform currents. Indeed, studies in both the relatively shallow water of the straits of Florida[8] and in deeper-water geostrophic flows[9] show how currents can produce substantial influences. Moreover, the importance of currents extends beyond specific ocean sites, as shown in certain acoustic interactions with the ocean bottom[4] and with mesoscale features.[10]

Among the recent experimental work surveyed by Ref.1, particular interest is noted in reciprocal transmissions (RT). These arise when two source-receiver pairs are used to transmit signals in opposite directions between two locations in an underwater channel. It can happen that the two signals show significant differences in phase and amplitude. Specifically, Refs.11 and 12 considered several RT examples and attributed the differences to the presence of currents. We note also that Ref.13 suggested that reciprocal differences in RT could be used to estimate components of tidal currents.

The wave equation and properties of its solutions in a medium moving with uniform velocity are well understood. One treatment of this situation may be found in Ref.14. However, if the medium moves with a nonuniform

velocity, the resulting equations and possible physical effects are much more complicated. The parabolic approximation in underwater acoustics[15] is attractive for considering nonuniform current effects, because of well-known advantages of this approximation. Little has been done in this area, although a parabolic approximation for sound propagation in a moving atmosphere has been examined.[16] Also, it has been shown[17] that certain numerical implementations of the parabolic approximation essentially satisfy acoustic reciprocity in the absence of currents, suggesting their possible application in RT where currents are present.

In this paper, we consider the effects of a depth-dependent, steady current upon received intensity, when a point source emits a cw signal. In Sec.I, we begin with the basic fluid-dynamical equations. After non-dimensionalizing and scaling, we derive an appropriate partial differential equation for the pressure field in the sound channel, including both current magnitude and current shear effects. Then, in Sec.II, we apply the parabolic approximation to this reduced equation. Depending on relative sizes of a current Mach number, a sound-speed deviation from a reference value, and a nondimensional measure of current gradient, six different parabolic equations are derived. Three of these equations explicitly include a term representing current gradient. For currents with a small shear parameter, the current gradient can be neglected, and the remaining terms lead naturally to an effective sound-speed profile (ESSP).

We study in Sec.III an isospeed sound channel with a lossy bottom and a shear current, using the ESSP and an existing numerical algorithm for the PE. The source is at a fixed depth for all computations. We first consider relative intensity and intensity differences for different currents and ranges out to 20 km. Calculations at source frequencies of 200 Hz and 500 Hz

show range intervals of substantial intensity differences between cases with oppositely directed currents. Next, we find that for a fixed range, relative intensities corresponding to different currents can vary enormously as the receiver changes depth. Finally, we examine relative intensity for currents varying between -1.0 ms^{-1} and 1.0 ms^{-1} at a number of ranges and depths and observe intensity variations of over 10 dB. We demonstrate that currents can induce large intensity differences in RT. Also, our numerical results indicate that the intensity variation with current speed, range, and depth is complex enough that no simple characterization of properties is possible.

I. MODEL FORMULATION

Consider an underwater sound channel as suggested in Fig.1(a). The origin of a Cartesian coordinate system $(\hat{x}, \hat{y}, \hat{z})$ lies on the channel surface, assumed horizontal, and the bottom is parallel to the surface. The $\hat{z}$-axis points towards the bottom and the $\hat{x}$-axis is in the vertical plane containing the acoustic source and receiver. The source $\mathcal{S}$ is at some depth $\hat{h}_S$ and emits a cw signal, while the point receiver $\mathcal{R}$ is at depth $\hat{h}_R$. The general governing equations[18] for the motion of an adiabatic and nondissipative fluid in the sound channel are:

$$\partial\hat{\rho}/\partial\hat{t} + \hat{\underset{\sim}{\nabla}} \cdot (\hat{\rho}\hat{\underset{\sim}{v}}) = 0 , \tag{1a}$$

$$\hat{\rho}D\hat{\underset{\sim}{v}}/D\hat{t} = - \hat{\underset{\sim}{\nabla}}\hat{p} \tag{1b}$$

and

$$\hat{c}^2 D\hat{\rho}/D\hat{t} = D\hat{p}/D\hat{t} , \tag{1c}$$

where $D/D\hat{t} = (\partial/\partial\hat{t} + \hat{\underset{\sim}{x}} \cdot \hat{\underset{\sim}{\nabla}})$. In Eqs.(1), $\hat{t}$ is time, $\hat{\underset{\sim}{\nabla}}$ is the gradient operator, $\hat{\rho}$ is fluid density, $\hat{\underset{\sim}{v}}$ is the fluid velocity vector, $\hat{p}$ is pressure, and $\hat{c}$ is sound speed. We use the convention of denoting

dimensional quantities by a caret. An equation for $\hat{c}$ in terms of thermodynamic state variables $\hat{\rho}$ and $\hat{p}$ may be appended to Eqs.(1) to obtain a system of six equations in six variables. Alternatively, $\hat{c}$ can be regarded as a specified function of space coordinates, so that Eqs.(1) are considered a closed system. We adopt this latter view as an appropriate one for some acoustic-propagation applications.

The quantities $\hat{\rho}$, $\hat{p}$, and $\hat{\underset{\sim}{v}}$ in Eqs.(1) are regarded as composed of ambient components, describing the state of the medium in the absence of an acoustic disturbance, plus acoustic perturbation components. The former are indicated by a zero subscript and the latter by a unit subscript, so that

$$\hat{\rho} = \hat{\rho}_o + \hat{\rho}_1 , \tag{2a}$$

$$\hat{p} = \hat{p}_o + \hat{p}_1 , \tag{2b}$$

and

$$\hat{\underset{\sim}{v}} = \hat{\underset{\sim}{v}}_o + \hat{\underset{\sim}{v}}_1 . \tag{2c}$$

We assume in this paper that any changes in $\hat{\rho}_o$ due to the current $\hat{\underset{\sim}{v}}_o$ are small enough to be neglected. Moreover, other spatial variations in $\hat{\rho}_o$ are regarded as small also, so that $\hat{\rho}_o$ is taken to be constant throughout the channel. Another motivation for this density assumption is the anticipation of parabolic approximations in Sec.II, which would be expected to reduce to the "standard" parabolic equation in the absence of currents. If density variations were included here, then, in the absence of currents, other parabolic equations would be obtained (see Ref.19) which have not yet been fully investigated or implemented. The ambient velocity $\hat{\underset{\sim}{v}}_o$ models the presence of a current. Its direction is in the horizontal ($\hat{x}$) direction, so it is confined to the source-receiver plane, and it may vary with depth as suggested by Fig.1(b). The sound-speed profile $\hat{c}(\hat{z})$ is also taken to

be depth dependent, as illustrated in Fig.1(c). Although our procedures may be applied to other and more general current and sound-speed structures, the case just described possesses many interesting features which will be discussed subsequently in this paper.

Now we proceed to nondimensionalize Eqs.(1) and (2). First, we let

$$\hat{x} = x\hat{L}, \quad \hat{y} = y\hat{L}, \quad \hat{z} = z\hat{L}, \quad \hat{t} = t\hat{T}, \tag{3}$$

where $\hat{L}$ and $\hat{T}$ are characteristic length and time scales to be specified later. Next, we let $\hat{U}_o$ and $\hat{c}_o$ be a reference current speed and sound speed, respectively. We scale the dependent variables by letting

$$\hat{\underset{\sim}{v}}_o(\hat{z}) = \hat{U}_o \underset{\sim}{v}_o(z) = \hat{U}_o u_o(z)\underset{\sim}{i}, \tag{4a}$$

$$\hat{\underset{\sim}{v}}_1(\hat{x},\hat{y},\hat{z}) = \delta_v \hat{c}_o \underset{\sim}{v}_1(x,y,z), \tag{4b}$$

and

$$\hat{\rho}_1(\hat{x},\hat{y},\hat{z}) = \delta_\rho \hat{\rho}_o \rho_1(x,y,z), \tag{4c}$$

where $\dot{u}_o$, v_1, and ρ_1 are dimensionless quantities of order of magnitude unity, $\underset{\sim}{i}$ is the unit vector along the x-axis, and δ_v and δ_ρ are small dimensionless numbers.

We substitute Eqs.(2) - (4) into Eq.(1a) to obtain

$$\hat{L}\hat{c}_o^{-1}\hat{T}^{-1}\partial\rho_1/\partial t + \underset{\sim}{\nabla} \cdot (M\underset{\sim}{v}_o + \delta_v\underset{\sim}{v}_1 + M\delta_\rho\rho_1\underset{\sim}{v}_o + \delta_\rho\delta_v\underset{\sim}{v}_1) = 0, \tag{5}$$

where M denotes the Mach number $\hat{U}_o/\hat{c}_o$. In the absence of any current, $M = 0$, and a linearized balance in Eq.(5) requires

$$\hat{L}\hat{c}_o^{-1}\hat{T}^{-1}\delta_\rho = \delta_v. \tag{6}$$

When Eq.(6) holds, the last term on the left of Eq.(5) is small and can be neglected. We note that in the absence of any acoustic perturbation, $\delta_v = \delta_\rho = 0$, and Eq.(5) is identically zero since $\hat{\underset{\sim}{v}}_o$ depends only on z and has no vertical component. Substituting Eq.(6) into Eq.(5), keeping terms of $0(\delta_v)$, we obtain

$$\mu \partial \rho_1 / \partial t + \underset{\sim}{\nabla} \cdot (\underset{\sim}{v}_1 + \mu M \rho_1 \underset{\sim}{v}_o) = 0 \, , \tag{7}$$

where

$$\mu = \hat{L} \hat{c}_o^{-1} \hat{T}^{-1} \, . \tag{8}$$

Since we anticipate that the parameter μ is order unity for acoustic waves, Eq.(7) represents a scaled conservation of mass equation.

Now we consider the scaling of Eq.(1b). The ambient pressure in the absence of an acoustic disturbance is scaled as

$$\hat{p}_o(\hat{x}, \hat{y}, \hat{z}) = \hat{\rho}_o \hat{U}_o^2 p_o(x, y, z) \, , \tag{9}$$

where p_o is dimensionless and order unity. As with the acoustic velocity and density, we set

$$\hat{p}_1(\hat{x}, \hat{y}, \hat{z}) = \delta_p \hat{\rho}_o \hat{c}_o \hat{L} \hat{T}^{-1} p_1(x, y, z) \, , \tag{10}$$

where p_1 is dimensionless and order unity and δ_p is a small dimensionless number. Thus, substituting into Eq.(1b) and algebraically simplifying, we obtain

$$(1 + \delta_\rho \rho_1)(\mu \delta_v \partial \underset{\sim}{v}_1 / \partial t + M^2 (\underset{\sim}{v}_o \cdot \underset{\sim}{\nabla}) \underset{\sim}{v}_o + M \delta_v (\underset{\sim}{v}_o \cdot \underset{\sim}{\nabla}) \underset{\sim}{v}_1$$
$$+ M \delta_v (\underset{\sim}{v}_1 \cdot \underset{\sim}{\nabla}) \underset{\sim}{v}_o + \delta_v^2 (\underset{\sim}{v}_1 \cdot \underset{\sim}{\nabla}) \underset{\sim}{v}_1) = - \underset{\sim}{\nabla}(M^2 p_o + \mu \delta_p p_1) \, . \tag{11}$$

In the absence of an ambient current $(M = 0)$, a linearized balance for acoustic perturbations requires

$$\delta_p = \delta_v . \tag{12}$$

Further, in the absence of any acoustic perturbation, $\delta_v = \delta_p = 0$, and the left side of Eq.(11) is identically zero since $\underset{\sim}{v}_o$ depends only on z and has no vertical component. Eliminating ambient terms as described from the linearized version of Eq.(11), we find

$$\mu \partial \underset{\sim}{v}_1 / \partial t + M(\underset{\sim}{v}_o \cdot \underset{\sim}{\nabla}) \underset{\sim}{v}_1 + M(\underset{\sim}{v}_1 \cdot \underset{\sim}{\nabla}) \underset{\sim}{v}_o = - \mu \underset{\sim}{\nabla} p_1 . \tag{13}$$

Finally, we scale Eq.(1c) in the same manner, using $n = \hat{c}_o / \hat{c}$ as the index of refraction. With the scaled variables already defined, Eq.(1c) becomes

$$n^{-2}(\mu \delta_\rho \partial \rho / \partial t + \delta_\rho M \underset{\sim}{v}_o \cdot \underset{\sim}{\nabla} \rho_1 + \delta_v \delta_\rho \underset{\sim}{v}_1 \cdot \underset{\sim}{\nabla} \rho_1) = M^3 \underset{\sim}{v}_o \cdot \nabla p_o + \mu M \delta_p \underset{\sim}{v}_o \cdot \underset{\sim}{\nabla} p_1$$

$$+ M^2 \delta_v \underset{\sim}{v}_1 \cdot \underset{\sim}{\nabla} p_o + \mu \delta_p \underset{\sim}{v}_1 \cdot \underset{\sim}{\nabla} p_1 + \mu^2 \delta_p \partial p_1 / \partial t . \tag{14}$$

When $\delta_v = 0$, the reduced equation is the balance condition to be satisfied identically by the ambient terms. Under the condition $\delta_v = 0(M^2)$, where as usual $M \ll 1$, the appropriate simplification of Eq.(1c) is

$$n^{-2}(\partial \rho_1 / \partial t + M \mu^{-1} \underset{\sim}{v}_o \cdot \underset{\sim}{\nabla} \rho_1) = \mu M \underset{\sim}{v}_o \cdot \underset{\sim}{\nabla} p_1 + \mu^2 \partial p_1 / \partial t . \tag{15}$$

That this condition on δ_v is reasonable follows from Eq.(4b), which implies that

$$\delta_v = 0(|\underset{\sim}{\hat{v}}_1|/\hat{c}_o) . \tag{16}$$

Since M in the ocean is never bigger than 10^{-3}, the condition $\delta_v = 0(M^2)$ and Eq.(16) imply that the magnitude of the velocity induced by the acoustic disturbance is no more than about 10^{-3} ms^{-1}. This is a reasonable and conservative estimate on the size of the induced current. Alternatively, it can be shown from Eqs.(4a) and (4b) that this condition means the

acoustically induced disturbance is smaller than the ambient flow by a scaling factor of order Mach number.

Equations (7), (13), and (15) represent scaled governing acoustic equations in our moving sound channel. There are two classical results which can be recovered from these equations. When $M = 0$, we have

$$\mu \partial \rho_1 / \partial t + \underset{\sim}{\nabla} \cdot \underset{\sim 1}{v} = 0 , \tag{17a}$$

$$\mu \partial \underset{\sim 1}{v} / \partial t = -\mu \underset{\sim}{\nabla} p_1 , \tag{17b}$$

and

$$n^{-2} \partial \rho_1 / \partial t = \mu^2 \partial p_1 / \partial t . \tag{17c}$$

An elementary manipulation of Eqs.(17) yields

$$\nabla^2 p_1 - (\mu^2 n^2) \partial^2 p_1 / \partial t^2 = 0 , \tag{18}$$

which is a scaled form of the wave equation in a stationary medium. In the event that $\underset{\sim o}{v}$ is a constant, it can also be shown that Eqs.(7), (13), and (15) reduce to

$$\nabla^2 p_1 - (\mu^2 n^2) [\partial/\partial t + (M/\mu) \underset{\sim o}{v} \cdot \underset{\sim}{\nabla}]^2 p_1 = 0 , \tag{19}$$

in agreement with Eq.(11.1.4) in Ref.14. Equation (19) is a scaled form of the modified wave equation which governs acoustic propagation in a medium moving with a steady, uniform velocity.

Next, we wish to extract from Eqs.(7), (13), and (15) a single equation for acoustic pressure. It is a straightforward calculation to show that these equations reduce to the pair

$$\nabla^2 p_1 = - 2(M/\mu) u_o' w_x + \mu^2 n^2 p_{1tt} + 2Mu_o \mu^2 n^2 p_{1xt} \tag{20a}$$

and

$$-p_{1zx} = w_t + (M/\mu) u_o w_x , \tag{20b}$$

where $u_o' = du_o/dz$, and $w = \underset{\sim}{v_1} \cdot \underset{\sim}{k}$ is the z-component of acoustic velocity $\underset{\sim}{v_1}$. The dimensionless ambient current component $u_o(z)$ is defined in Eq. (4a). Now, by taking the t-derivative of Eq. (20a) and the x-derivative of Eq. (20b), the w term can be eliminated to give the following third order equation, correct to terms of order M:

$$\nabla^2 p_{1t} - \mu^2 n^2 p_{1ttt} - 2M u_o \mu n^2 p_{1xtt} - 2(M/\mu) u_o' p_{1zx} = 0 . \tag{21}$$

Since the source has been assumed to emit a cw signal, p_1 has the form

$$p_1 = A(x, y, z) e^{-i\omega t} , \tag{22}$$

where $\omega = \hat{\omega}\hat{T}$ is scaled frequency and $\hat{\omega}$ is frequency in radians. Substituting Eq. (22) into Eq. (21) gives

$$\nabla^2 A + \omega^2 \mu^2 n^2 A + 2i M u_o/\mu \omega n^2 A_x - 2i(M/\mu\omega) u_o' A_{zx} = 0 . \tag{23}$$

This result may be thought of as having three components. First, when $M = 0$, we recover the principal constituent

$$\nabla^2 A + \omega^2 \mu^2 n^2 A = 0 , \tag{24}$$

which is the Helmholtz equation. The remaining components are $O(M)$ corrections to the Helmholtz equation. One of these, the third term in Eq. (23), depends directly upon the current u_o and the x-derivative of pressure A. The other, the fourth term in Eq. (23), depends upon the current gradient u_o' and a mixed derivative of A. Note that the sound-speed gradient is not present in Eq. (24).

We are now able to make appropriate choices for the length and time scales introduced earlier. Picking $\hat{\omega}^{-1} = \hat{T}$ ensures that time derivatives are $O(1)$, since the scaled frequency is $\omega = 1$. The choice $\hat{L} = \hat{c}_o / \hat{\omega}$ then gives us the inverse wavenumber $\hat{k}_o$ as our length scale. Consequently, $\mu = 1$, and Eq.(23) simplifies to

$$\nabla^2 A + n^2 A + 2iMn^2 u_o A_x - 2iMu_o' A_{zx} = 0 .\tag{25}$$

II. THE PARABOLIC APPROXIMATION

In order to generate a parabolic approximation to Eq.(25), we first convert to cylindrical coordinates. These are $(\hat{r}, \theta, \hat{z})$ in dimensional form, or (r, θ, z) in dimensionless form, where θ is measured from the x-axis. In terms of the independent variables r, θ, and z, Eq.(25) in the x-z plane $(\theta = 0)$ is

$$A_{rr} + r^{-1} A_r + A_{zz} + r^{-2} A_{\theta\theta} + n^2 A + 2iMu_o n^2 A_r - 2iMu_o' A_{rz} = 0 .\tag{26}$$

An essential feature of the parabolic approximation[15] is the far-field assumption. We make first the usual assumption of a forward-propagating wave,

$$A = \psi(r,z) H_o^{(1)}(r) ,\tag{27a}$$

where $H_o^{(1)}(r)$ is the Hankel function of the first kind of order zero. For $H_o^{(1)}(r)$ we use the expression[20]

$$H_o^{(1)}(r) = \sigma r^{-1/2} e^{ir} [1 - i/8r + o(r^{-2})] ,\tag{27b}$$

where σ is a constant. We remark that the second term on the right side of Eq.(27b) is not retained in Ref.15. although its presence here is useful in our scaling arguments and facilitates a validity condition

of the parabolic approximation. As in Ref.15, we assume θ-derivatives are typically $O(1)$. For our assumptions on the current and sound-speed structures and for many types of boundary conditions, scaling arguments can be used to conclude that $\psi_{\theta\theta}$ is $O(1)$ near the source-receiver plane. Substituting Eqs.(27) into Eq.(26) and keeping terms multiplied by $1/r$, but neglecting those multiplied by $1/r^2$, we obtain

$$\psi_{rr} - i(8r)^{-1}\psi_{rr} + 2i\psi_r + (4r)^{-1}\psi_r + \psi_{zz} - i(8r)^{-1}\psi_{zz} + [(n^2 - 1) + ir^{-1}(n^2 - 1)]\psi$$
$$+ 2iMu_o n^2[\psi_r - i(8r)^{-1}\psi_r - 3(8r)^{-1}\psi + i\psi]$$
$$- 2iMu_o'[\psi_{zr} - i(8r)^{-1}\psi_{zr} - 3(8r)^{-1}\psi_z + i\psi_z] = 0 . \tag{28}$$

To proceed further, we need to estimate the sizes of terms in Eq.(28). For this purpose, we first write

$$n^2 - 1 = (\hat{c}_o + \hat{c})(\hat{c}_o - \hat{c})/\hat{c}^2 . \tag{29a}$$

We recall that the choice of $\hat{c}_o$ is arbitrary, and for numerical examples in Sec.III, we choose $\hat{c}_o = 1500 \text{ ms}^{-1}$. If we let

$$\epsilon = \max|\hat{c}_o - \hat{c}|/\hat{c}_o , \tag{29b}$$

where the maximum is taken over depth $\hat{z}$, then ϵ is a small dimensionless number, typically ranging from 0.03 in some deep-water cases to as small as zero in an isospeed channel (with $\hat{c}_o = \hat{c}$). This parameter represents the largest deviation in sound speed from the reference value in the channel. We can then rewrite Eq.(29a) as

$$n^2 - 1 = \epsilon\eta(z) \tag{29c}$$

where $\eta(z)$ is a function of order of magnitude unity. It follows that $\eta(z)$ is given by

$$\eta(z) = \frac{\hat{c}_o - \hat{c}(z)}{\max\left|\hat{c}_o - \hat{c}(z)\right|} + 0(\epsilon) \ . \tag{29d}$$

Next, we rescale the current gradient u'_o to indicate its actual magnitude. This is necessary because small currents may give rise to rather large current shears. Thus, we express the current gradient as

$$u'_o = \zeta G' , \tag{30a}$$

where G' is an order unity function. One way to define the parameter ζ is as the maximum of u'_o over all depths z. In order to indicate possible values for ζ, we consider that depth at which maximum current shear occurs. In the vicinity of this depth, $G' \cong 1$ (so that $\zeta \cong u'_o$). In particular, our scaling can be used to express u'_o as

$$u'_o = \hat{L}\hat{U}_o^{-1} d\hat{u}_o/d\hat{z} = (\hat{c}_o/2\pi\hat{f}\hat{U}_o)(d\hat{u}_o/d\hat{z}) , \tag{30b}$$

where the second equation in Eq.(30b) follows from our choice of $\hat{L}$, and $\hat{f}$ is source frequency in hertz. In a typical example of large current shear discussed in Ref.21, $d\hat{u}_o/d\hat{z} = 0.03 \ s^{-1}$ with a surface current speed of $\hat{U}_o = 0.3 \ ms^{-1}$. It follows that in this example, Eqs.(40a) and (40b) yield the estimate

$$\zeta \cong 25/\hat{f} . \tag{30c}$$

Consequently, ζ is an order-unity parameter at lower acoustic frequencies, and remains considerably bigger than the Mach number at mid-frequencies. It will be shown subsequently that the possibility of such values for ζ can significantly influence the potential parabolic approximations.

When the two scales ϵ and ζ are introduced into Eq.(28), all the coefficients become appropriately scaled. We seek to balance ψ_r and ψ_{zz}

terms, since they are leading terms in the parabolic equation. There are also terms with coefficients like r^{-1}, which we wish to neglect. This suggests expressing the nondimensional variables r and z in terms of new scaled variables r' and z' as follows:

$$r = r_o + r'\delta^{-1}. \tag{31a}$$

and

$$z = z'\delta^{-1/2}, \tag{31b}$$

where the parameters $r_o > 0$ and δ will be selected as a consequence of balancing requirements. We then substitute Eqs.(29c), (30a), and (31) into Eq.(28) and set $r' = 0$. This value for r' is appropriate because any balancing must hold at the minimum range $r = r_o$. We obtain

$$\delta^2\psi_{r'r'} - \delta^2 i(8r_o)^{-1}\psi_{r'r'} + 2i\delta\psi_{r'} + \delta(4r_o)^{-1}\psi_{r'} + \delta\psi_{z'z'} - i\delta(8r_o)^{-1}\psi_{z'z'}$$
$$+ \epsilon\eta\psi + \epsilon i\eta r_o^{-1}\psi + 2i(1+\epsilon\eta)Mu_o[\delta\psi_{r'} - i(8r_o)^{-1}\delta\psi_{r'} - 3(8r_o)^{-1}\psi + i\psi]$$
$$- 2iM\zeta G'[\delta^{3/2}\psi_{z'r'} - i(8r_o)^{-1}\delta^{3/2}\psi_{z'r'} - 3(8r_o)^{-1}\delta^{1/2}\psi_{z'} + i\delta^{1/2}\psi_{z'}] = 0. \tag{32}$$

Examination of Eq.(32) shows that parabolic approximations are found by keeping terms of $O(\delta)$ and neglecting terms of $O(\delta^2)$. Furthermore, omitting terms with r_o^{-1} coefficients suggests that we require $r_o = O(\delta^{-1})$. This provides one possible lower limit in range for application of the parabolic approximations. Anticipating our choice of δ, we also note that terms like $\epsilon\delta$ and $M\delta$ will be negligibly small compared to either ϵ, δ, or M, and so Eq.(32) reduces to

$$2i\psi_{r'} + \psi_{z'z'} + \epsilon\eta\delta^{-1}\psi - 2M\delta^{-1}u_o\psi + 2M\zeta\delta^{-1/2}G'\psi_{z'}$$
$$= O(\delta, M, \epsilon, \epsilon M\delta^{-1}, M\zeta\delta^{1/2}). \tag{33}$$

The appropriate choice of δ is now determined by the relative sizes of ϵ, M, and ζ in Eq.(33).

Suppose first that $M \geq O(\epsilon^{1/2})$. This type of parameter relationship might exist in a moving isospeed, or nearly isospeed, channel, for example, where ϵ is zero or nearly so. The proper balance of terms imposes $\delta = M$, and we obtain from Eq.(33)

$$2i\psi_{r'} + \psi_{z'z'} - 2u_o\psi + 2\zeta M^{1/2}G'\psi_{z'} = O(M) . \qquad (34a)$$

This new parabolic approximation permits both current magnitude and current shear to influence sound propagation. Retention of the fourth term on the left of Eq.(34a) depends upon the size of ζ. Since terms of $O(M)$ have been neglected, it follows that Eq.(34a) is appropriate for $\zeta M^{1/2} > O(M)$, i.e., $\zeta > O(M^{1/2})$. For ζ smaller, i.e., $\zeta \leq O(M^{1/2})$, then Eq.(34a) reduces to

$$2i\psi_{r'} + \psi_{z'z'} - 2u_o\psi = O(M) . \qquad (34b)$$

We described a specific example of current shear previously. Let us use numerical values from that example, along with one natural form of the order condition $\zeta > O(M^{1/2})$. Equation (30c) implies for this example that for frequencies less than about 800 Hz, the shear term should be kept in the parabolic equation. Many applications involve frequencies that are substantially lower than this. Therefore, the presence of the shear term in Eq.(34a) could be significant.

Now we consider the possibility of slightly larger relative sound-speed variations, with $O(\epsilon) \leq M < O(\epsilon^{1/2})$. In this situation, the current term in Eq.(33) still tends to dominate the sound-speed term, but the latter is no longer smaller than previously neglected terms. Consequently, the proper balance of terms continues to imply $\delta = M$, and Eq.(33) becomes

$$2i\psi_{r'} + \psi_{z'z'} + \epsilon M^{-1}\eta\psi - 2u_o\psi + 2\zeta M^{1/2}G'\psi_{z'} = O(M) . \qquad (35a)$$

Equation (35a) is another new parabolic approximation, containing effects of three mechanisms: sound-speed variation, current magnitude, and current shear. As before, Eq.(35a) is appropriate for $\zeta > O(M^{1/2})$. For smaller current shears, Eq.(35a) reduces to

$$2i\psi_{r'} + \psi_{z'z'} + \epsilon M^{-1}\eta\psi - 2u_o\psi = O(M) . \qquad (35b)$$

This equation shows that current-magnitude effects can influence the parabolic approximation in a way directly analogous to sound-speed variations, as will be further discussed later.

Next, we consider the case where $O(\epsilon^2) < M \leq O(\epsilon)$. As for the previous cases, there are physical situations which correspond to this parameter relationship. For example, a shallow-water channel located in a temperate latitude might have a small relative sound-speed deviation during the colder months, and this deviation may be comparable in size to the Mach number of a tidal current in the channel. Given this parameter relationship, a proper balance of terms in Eq.(33) now occurs when $\delta = \epsilon$. Neglecting small terms as before, we obtain

$$2i\psi_{r'} + \psi_{z'z'} + \eta\psi - 2M\epsilon^{-1}u_o\psi + 2M\epsilon^{-1/2}\zeta G'\psi_{z'} = O(\epsilon) . \qquad (36a)$$

The same physical terms are retained in Eq.(36a), but now with a slightly different order condition for neglected terms. Whether the current shear term should be kept again depends upon whether its asymptotic order is larger than neglected terms, i.e., $\zeta > O(\epsilon^{3/2}M^{-1})$. For example, if $M = O(\epsilon)$, then this condition is $\zeta > O(\epsilon^{1/2})$, while if $M = O(\epsilon^{3/2})$, ζ should be order one. Clearly, the shear term becomes potentially more significant as

current strength increases. On the other hand, if the shear term is suffi-ciently small, it follows that

$$2i\psi_{r}{}' + \psi_{z}{}'_{z}{}' + \eta\psi - 2M\epsilon^{-1}u_{o}\psi = O(\epsilon) . \tag{36b}$$

Finally, we note the remaining case when $M \leq O(\epsilon^{2})$. This situation might arise in a deep ocean channel with a large relative sound speed deviation. Once again, $\delta = \epsilon$, and from Eq.(33),

$$2i\psi_{r}{}' + \psi_{z}{}'_{z}{}' + \eta\psi + 2M\epsilon^{-1/2}\zeta G'\psi_{z}{}' = O(\epsilon) . \tag{37a}$$

The current magnitude term $2M\epsilon^{1/2}u_{o}\psi$ that was present in Eq.(36a) is absent in Eq.(37a). Consequently, in this case the current structure has no explicit effect upon sound propagation in the channel. However, it is still possible for the current shear to affect the propagation, in the situation $\zeta > O(\epsilon^{3/2}M^{-1})$. If ζ is small enough, then the shear term can also be neglected, and Eq.(33) reduces to

$$2i\psi_{r}{}' + \psi_{z}{}'_{z}{}' + \eta\psi = O(\epsilon) , \tag{37b}$$

which is the scaled form of the standard PE in Ref.15.

The parabolic equations which we have developed above may be written in dimensional form as follows. First, Eq.(34a) becomes

$$2i\hat{k}_{o}\hat{\psi}_{\hat{r}} + \hat{\psi}_{\hat{z}\hat{z}} - 2\hat{k}_{o}^{2}(\hat{u}_{o}/\hat{c}_{o})\hat{\psi} + (2/\hat{c}_{o})(d\hat{u}_{o}/d\hat{z})\hat{\psi}_{\hat{z}} = 0 , \tag{38a}$$

where dimensional ambient current component $\hat{u}_{o}(\hat{z}) = \hat{U}_{o}u_{o}(z)$. In addition to the usual single-r and double-z derivative terms in Eq.(38a), there are two other terms, due to current shear and current magnitude. For brevity, we refer to these two contributions as CS and CU, respectively. Equation (34b) is

$$2i\hat{k}_o\hat{\psi}_{\hat{r}} + \hat{\psi}_{\hat{z}\hat{z}} - 2\hat{k}_o^2(\hat{u}_o/\hat{c}_o)\hat{\psi} = 0 , \tag{38b}$$

which contains only CU. The dimensional forms of both Eqs.(35a) and (36a) are the same:

$$2i\hat{k}_o\hat{\psi}_{\hat{r}} + \hat{\psi}_{\hat{z}\hat{z}} + \hat{k}_o^2(n^2 - 1)\hat{\psi} - 2\hat{k}_o^2(\hat{u}_o/\hat{c}_o)\hat{\psi} + (2/\hat{c}_o)(d\hat{u}_o/d\hat{z})\hat{\psi}_{\hat{z}} = 0 . \tag{39a}$$

This parabolic equation contains CS and CU and an additional term arising from sound-speed variations, abbreviated by SS. Similarly, Eqs.(35b) and (36b) lead to the same result

$$2i\hat{k}_o\hat{\psi}_{\hat{r}} + \hat{\psi}_{\hat{z}\hat{z}} + \hat{k}_o^2(n^2 - 1)\hat{\psi} - 2\hat{k}_o^2(\hat{u}_o/\hat{c}_o)\hat{\psi} = 0 , \tag{39b}$$

possessing both CU and SS. Finally, Eqs.(37a) and (37b) become

$$2i\hat{k}_o\hat{\psi}_{\hat{r}} + \hat{\psi}_{\hat{z}\hat{z}} + \hat{k}_o^2(n^2 - 1)\hat{\psi} + (2/\hat{c}_o)(d\hat{u}_o/d\hat{z})\hat{\psi}_{\hat{z}} = 0 \tag{40a}$$

and

$$2i\hat{k}_o\hat{\psi}_{\hat{r}} + \hat{\psi}_{\hat{z}\hat{z}} + \hat{k}_o^2(n^2 - 1)\hat{\psi} = 0 . \tag{40b}$$

The former has CS plus SS, while the latter has only SS.

Equations (38a) - (40b) represent the six parabolic approximations that incorporate all appropriate combinations of the physical mechanisms represented by terms that we denote by CS, CU, and SS. Moreover, in addition to these results, our derivations have determined ordering conditions on the parameters M, ϵ, and ζ which give asymptotic regions of validity for our equations. We next present one way to illustrate these regions, and indicate the corresponding parabolic approximations by our Fig.2. Possible values of M, ϵ, and ζ occupy one octant of a three-dimensional parameter space. Figure 2 represents a planar section of this three-dimensional space, formed by the plane $\zeta = \zeta_o$, where ζ_o is an arbitrary value of the

current-shear parameter. Region I represents values $M \geq O(\varepsilon^{1/2})$ and includes the isospeed channel ($\varepsilon = 0$) as a subcase. Parabolic approximations in I contain CU but not SS. Region II corresponds to values with $O(\varepsilon^{1/2}) > M > O(\varepsilon^2)$. It includes sound channels with both currents and moderate sound-speed deviations, such as those that might occur in a fairly shallow ocean in cooler months. Parabolic approximations in II contain both CU and SS. Finally, Region III embraces $M \leq O(\varepsilon^2)$ and such physical situations as a deep ocean SOFAR channel. Region III parabolic approximations include SS but not CU. We note that our examples suggest that in a very general sense, the transition from Region I to III corresponds to a transition from shallow to deep sound channels. Each region in Fig. 2 is further divided into subregions A and B, corresponding to locations of higher and lower shear, respectively. The dashed curve is the intersection of the plane $\zeta = \zeta_0$ with the surface in (ε, M, ζ)-space which forms the subregions A and B. In Region I and that portion of Region II indicated, this surface is expressed as $\zeta_0 = M^{1/2}$, and in the remainder of Region II and Region III, the equation is $\zeta_0 = \varepsilon^{3/2} M^{-1}$. The subregions below the dashed curve are regions of relatively higher shear, while those above the curve have relatively lower shear. As seen in our derivations previously, the importance of current shear in the A subregions is manifested by the inclusion of CS in the parabolic approximations. Figure 2 shows all relevant terms, using our notations, in the various subregions. We remark that for different values of ζ_0, the position of the dashed curve would be different. Also, we mention that the boundary curves of the various subregions have been determined as asymptotic order conditions, and as such are "fuzzy" rather than sharp. We choose to represent them in Fig. 2 as sharp curves only to aid visualization of the validity regimes.

It is important to note that Eqs.(38b) and (39b) can be transformed into a form suitable for analysis and solution by existing numerical algorithms for the parabolic equation. That is, both these equations can be converted into the form of Eq.(40b) by introducing an effective sound speed $\tilde{c}$. This quantity should be defined by the following equation:

$$(\hat{c}_o/\tilde{c})^2 - 1 = (\hat{c}_o/\hat{c})^2 - 1 - 2\hat{u}_o/\hat{c}_o . \tag{41a}$$

Solving for $\tilde{c}$, we have

$$\tilde{c} = \hat{c}[1 - (2\hat{u}_o/\hat{c}_o)(\hat{c}/\hat{c}_o)^2]^{-1/2} , \tag{41b}$$

or, to first order in Mach number,

$$\tilde{c} \cong \hat{c}[1 + \hat{u}_o/\hat{c}_o] . \tag{41c}$$

An alternative form which is a consistent approximation of Eq.(41c) is

$$\tilde{c} \cong \hat{c} + \hat{u}_o . \tag{41d}$$

Equation (41d) expresses the effective sound speed profile (ESSP) as the actual sound speed shifted by the current. If Eq.(41a) is substituted into Eqs.(38b) or (39b), the result is

$$2i\hat{k}_o\hat{\psi}_r + \hat{\psi}_{\hat{z}\hat{z}} + \hat{k}_o^2(\tilde{n}^2 - 1)\hat{\psi} = 0 , \tag{41e}$$

where $\tilde{n} = \hat{c}_o/\tilde{c}$. The form of Eq.(41e) is exactly the same as Eq.(40b). Consequently, presently available numerical algorithms for solving Eq.(40b) are capable of predicting current effects in low-shear channels, once the current is incorporated into the sound speed profile using Eq.(41d). Similarly, CU and SS in Eq.(39a) can be combined, and CU in Eq.(38a) is mathematically equivalent to SS in Eq.(40a). In all cases, any current effects on initial and boundary conditions are assumed negligible.

Notwithstanding the analogous effects of CU and SS, it is important to note that the presence of CS in Eqs.(38a), (39a), and (40a) requires modifications in existing parabolic-approximation algorithms for their numerical solution.

III. NUMERICAL RESULTS

In this section, we demonstrate the acoustic importance of ocean currents by calculating transmission loss for an example sound channel. This channel is depicted in Fig.3(a). A point source $\mathscr{S}$ emits a cw signal and is located at a depth of 25 m. The receiver $\mathscr{R}$ is at depth $\hat{h}_R$, and the channel depth is 100 m. The sound speed is taken to be constant throughout the water, and $\hat{c}_o = \hat{c} = 1500$ ms^{-1}. As specified earlier for models in this paper, we assume a steady horizontal current in the $\mathscr{S}$-$\mathscr{R}$ plane. As suggested in Fig.3(b), the current component $\hat{u}_o$ is chosen to decrease linearly from its value at the surface to zero at mid-depth, and remains zero from mid-depth to the bottom of the channel. We use the surface speed for the reference current speed, i.e., $\hat{U}_o = |\hat{u}_o(0)|$. As discussed at the end of Sec.II, the current structure induces an ESSP in the channel. The exact sound-speed profile is shown in Fig.3(c). The ESSP, computed from Eq.(41d), is shown in Fig.3(d). For example, for a surface-current component of 1.0 ms^{-1}, the ESSP is 1501 ms^{-1} at the surface and 1500 ms^{-1} at mid-depth and below. If the surface-current component is -1.0 ms^{-1}, the ESSP is 1499 ms^{-1} at the surface and 1500 ms^{-1} at mid-depth and below. These cases are sketched as large-dashed and small-dashed lines, respectively, in Figs.3(b) and 3(d). The parameter values are $\epsilon = 0$ and $M = 6.7 \times 10^{-4}$. For the lowest source frequency ($\hat{f} = 200$ Hz) used in this example, $\zeta = 2.4 \times 10^{-2}$. Thus, $\zeta \le O(M^{1/2})$, and Region IB is appropriate.

The numerical algorithm used in this example to solve Eq.(41e) is described in Ref.22. Using an implicit finite difference (IFD) scheme, the algorithm solves standard parabolic equations of the form of Eq.(41e). The formulas of Eqs.(41a) - (41d) show that Eq.(38b) can be transformed into Eq.(41e) via the introduction of an ESSP. Computation of the solution requires specification of boundary and initial conditions. We assume a pressure release condition at the upper ocean surface and a lossy bottom, which extends 150 m below the channel bottom as suggested in Fig.3(a). The bottom parameters were selected to correspond to an isospeed example presented in Refs.22 and 23. The sound speed in the bottom is 1550 ms^{-1}, the bottom density is 1.2 gcm^{-3}, and the attenuation is 1 dB/wavelength. The model introduces an artificial strongly-absorbing layer of an additional 100 m depth beyond the assumed bottom. Also, it supplies one necessary matching condition of the nearfield and farfield solutions, using a Gaussian source distribution to describe the acoustic field near the source. Relevant numerical parameters, such as depth and range mesh sizes, are identical to those used in Ref.22. The numerical quantity computed is relative intensity of the received signal, denoted by I:

$$I = 10 \ \log_{10}\left(\hat{p}(\hat{r},\hat{z})/\hat{p}_{ref}\right)^2 . \tag{42a}$$

In Eq.(42a), $\hat{p}_{ref}$ is the acoustic pressure generated by the signal at $\hat{r} = 1$ m, and

$$\hat{p}(\hat{r},\hat{z}) = \hat{\psi}(\hat{r},\hat{z})H_o^{(1)}(\hat{k}_o\hat{r}) , \tag{42b}$$

which is the dimensional form of Eq.(27a).

Figure 4 is a plot of relative intensity for a signal $\hat{f} = 200$ Hz, shown to a range of 20 km. For brevity we define $\hat{u}_o(0) = \hat{u}_{oo}$. The solid curve I_1 is the result when $\hat{u}_{oo} = 0$, i.e., corresponding to an isospeed channel with no ambient current. The long-dashed curve I_2 results when $\hat{u}_{oo} = 1.0$ ms^{-1}, while the short-dashed curve I_3 is for $\hat{u}_{oo} = -1.0$ ms^{-1}. For all three curves, there is a general tendency for intensity to decrease with range. Of course, this is because of cylindrical spreading from the Hankel function in Eq.(42b). As range increases from 2 im, the three curves remain quite close, out to about 6 km. At this range, the no-current case I_1 undergoes a sharp fade to -119 dB. By contrast, both I_2 and I_3 remain at about -80 dB. As range continues to increase, significant differences continue to appear in the curves. For $\hat{u}_{oo} = 1.0$ ms^{-1}, I_2 appears to show a shift toward the source relative to I_1, while I_3 for $\hat{u}_{oo} = -1.0$ ms^{-1} shifts away from the source. This shifting, in addition to differences in the shapes of the curves, can account for sizeable differences in relative intensity at certain ranges. For example, at $\hat{r} = 13$ km, I_1 is about -74 dB, I_2 is about -88 dB at the bottom of a fade, and I_3 is decreasing and is about -69 dB. Thus, at this range, a current of plus (or minus) 1.0 ms^{-1} causes an intensity drop (or increase) of 14 dB (or 5 dB). Furthermore, it is significant that intensity differences of several dB are not confined to isolated points, but are maintained over range intervals of a few km. On the other hand, there are range intervals where intensity differences due to currents are small, such as near $\hat{r} = 11.5$ km where the three curves almost simultaneously intersect. However, in contrast to range intervals of large intensity differences, those of small intensity differences tend to be smaller, of the order of hundreds of meters. These observations shed light on some aspects of reciprocal

transmissions (RT). Since $\mathscr{J}$ and $\mathcal{R}$ are at equal depths in Fig.4, switching their respective locations is equivalent to reversing the direction of the current. Thus, the difference between the short-dashed and long-dashed curves predicts the measured intensity difference of the signals between $\mathscr{J}$-$\mathcal{R}$ pairs placed in a current of 1.0 ms^{-1} magnitude at the surface. As mentioned previously, these differences can be large at certain points, can exceed several dB over large range intervals, and are small over some other intervals.

Intensity differences are emphasized in Fig.5. The three curves shown here represent signed differences among the three curves which are shown separately in Fig.4. The solid- and long-dashed curves show intensity differences from the no-current case (I_1) when the current is present and is either 1.0 ms^{-1} or -1.0 ms^{-1} at the surface. As observed more clearly than in Fig.4, there are large range intervals possessing significant intensity differences. The short-dashed curve, as the difference between I_2 and I_3 in Fig.4, represents the intensity difference of RT. For ranges beyond 6 km, this curve exhibits range intervals of not insignificant length, in which net difference in signal intensity is several dB. Moreover, at particular range values, such as $\hat{r} = 13.5$, 14.5, 17.5, and 18 km, intensity differences are almost 20 dB. Although the three curves in Fig.5 are not periodic, the patterns are roughly accounted for by the shifting of the no-current intensity curve described in connection with Fig.4.

In Fig.6, we again plot relative intensity for three cases. As in Fig.4, I_1 corresponds to $\hat{u}_{oo} = 0$, I_2 to $\hat{u}_{oo} = 1.0$ ms^{-1}, and I_3 to $\hat{u}_{oo} = -1.0$ ms^{-1} for $\hat{f} = 200$ Hz. However, the receiver is now located at the bottom of the channel (where $\hat{h}_R = 100$ m), as opposed to Fig.4 where $\hat{h}_R = 25$ m. There are significant differences between Figs.4 and 6. All three curves in Fig.6

are shifted downward approximately 15 dB from those in Fig.4. This results

from the fact that the receiver in the latter figure is on the interface

of a considerably lossy bottom. As in Fig.4, these curves track each other

closely for small values of $\hat{r}$, and current effects become apparent beyond

6 km. However, the rough shifting of the no-current curve by the presence

of current, which was readily seen in Fig.4, is more irregular in Fig.6.

When $\hat{u}_{oo} = 1.0$ ms^{-1}, there are two extremely deep fades, one at about 12 km

(to -135 dB) and the second at about 19 km (to -129 dB). In Fig.4, current

values did not induce such deep fades for the range values examined. We

remark that as in Fig.4, there are several range intervals which contain

large intensity differences. Finally, we indicate that nothing can be

said about RT in Fig.6, because the source and receiver are at different

depths for calculations shown.

In Fig.7, the receiver depth is again 25 m, but now the source

frequency is $\hat{f} = 500$ Hz, instead of $\hat{f} = 200$ Hz as in Fig.4. As in both

Figs.4 and 6, the solid curve represents the relative intensity in the

absence of any current, while the long- and short-dashed curves represent

surface currents of 1.0 ms^{-1} and -1.0 ms^{-1}, respectively. We note the

noisier behavior of intensity at the higher frequency in Fig.7, and observe

that the overall pattern of the curves is notably more complex than in

either Figs.4 or 6. For small ranges, the curves nearly coincide, as

observed in earlier cases. At about $\hat{r} = 5$ km, we observe a separation in

the curves, indicating that current effects begin to be noticeable at a

shorter range than when $\hat{f} = 200$ Hz. Moreover, instead of the current

producing a rough shift to the left or right of the solid curve, a general

shift upward or downward is seen. When $\hat{u}_{oo} = -1.0$ ms^{-1}, there is an overall shift upwards of several dB, while in contrast, a general shift downward by a somewhat larger amount occurs for $\hat{u}_{oo} = 1.0$ ms^{-1}. Beyond about 15 km, intensity shifts can be very dramatic. For instance, the difference between I_2 and I_3 is at least 5 dB, with a maximum of about 20 dB near 19 km. We recall that when $\hat{u}_{oo} = -1.0$ ms^{-1}, the current induces an ESSP which possesses a positive gradient down to mid-depth, while when $\hat{u}_{oo} = 1.0$ ms^{-1}, the ESSP has a negative gradient. In terms of ray theory, which is reasonably accurate at the higher frequency used in Fig.7, we would expect the negative gradient to refract more rays to the bottom than would otherwise occur in the absence of any current. Similarly, the positive gradient would tend to refract rays upward. Since the assumed bottom is lossy, particularly at higher frequencies, we would expect to observe higher intensities for negative currents and lower intensities for positive currents. This is exactly the qualitative effect visible in Fig.7. It is interesting to note that the same features are not evident at these ranges for the lower frequency used in the comparable Fig.4.

Figure 8(a) depicts the relative intensity versus receiver depth $\hat{h}_R$ for $\hat{f} = 200$ Hz and a range of $\hat{r} = 7$ km. Each curve corresponds to a different current, and as before I_1 results from no current, I_2 from $\hat{u}_{oo} = 1.0$ ms^{-1}, and I_3 from $\hat{u}_{oo} = -1.0$ ms^{-1}. Figure 8(b) is analogous, but is for $\hat{r} = 10$ km. In both figures, the intensity drops sharply near both the surface and the bottom. At the former location, the pressure-release condition accounts for the drop at the surface, while the lossy bottom accounts for the decrease in intensity there. The overall downward shift of intensity at $\hat{h}_R = 100$ m, which was noted in Fig.6, is apparent in Fig.8(a), but is absent in Fig.8(b). This happens at $\hat{r} = 10$ km because all three intensities are near

fades for $\hat{h}_R = 25$ m (see Fig.4), while at $\hat{h}_R = 100$ m, the intensities are all approaching peaks (see Fig.6). Consequently, the decrease near $\hat{h}_R = 100$ m in Fig.8(b) is to a relative, rather than an absolute, minimum of the intensity curves. In Fig.8(a), the maximum intensity difference between I_2 and I_3 is about 15 dB and occurs near $\hat{h}_R = 100$ m. Also at $\hat{h}_R = 40$ m, all three curves intersect, so that neither current induces any intensity change. In contrast, Fig.8(b) shows the largest intensity difference of about 20 dB at $\hat{h}_R = 30$ m, and the curves nearly coincide at the bottom.

In Fig.9, we plot relative intensity versus surface current component $\hat{u}_{oo}$ for six values of source-receiver range. The receiver depth is 25 m, as is the source depth, and $\hat{f} = 200$ Hz. The effect of varying magnitude and sign of $\hat{u}_{oo}$ has remarkably different effects at different ranges. As $\hat{u}_{oo}$ varies from -1.0 ms^{-1} to 1.0 ms^{-1}, the intensity changes almost linearly at 5, 7, 8, and 9 km. The intensity decreases about 2 dB at 5 and 8 km, decreases 4 dB at 9 km, and increases 2 dB at 7 km. This behavior contrasts with that at 6 km and 10 km. At 6 km, the intensity drops sharply as the current increases from $\hat{u}_{oo} = -1.0$ ms^{-1}. When the surface current reaches zero, intensity drops to -119 dB, a change of over 40 dB. As $\hat{u}_{oo}$ increases towards 1.0 ms^{-1}, intensity increases. At that speed, the intensity differs from that at $\hat{u}_{oo} = -1.0$ ms^{-1} by 2 dB. For $\hat{r} = 10$ km, intensity continually increases as the current increases, and the net change in intensity between the two currents is about 15 dB.

Several observations can be made about RT in light of results in Fig.9. Suppose there were two source-receiver pairs submerged at 25 m depth in this channel, so that the source-receiver direction parallels the current direction. If the surface current component were 1.0 ms^{-1} for one $\mathscr{S}$-$\mathscr{R}$ pair, then it would be -1.0 ms^{-1} for the reciprocal pair. For differing range

between the pairs, the intensity differences measured at each receiver would also be expected to change. At a separation of 5 km, the intensity difference at both ends of the figure is about 2 dB, while at 10 km, the difference is about 15 dB. Note that at 6 km, the intensity difference between the receivers is only about 2 dB, despite the fact that the relative intensity undergoes its greatest variation with current at this range. Now suppose that the surface-current speed is halved, to 0.5 ms^{-1}. At 5, 6, 7, and 8 km, the intensity difference measured between the two receivers from Fig.9 is only 1 dB or smaller. At 9 km, the difference is 2 dB, and at 10 km, the difference is as great as 7 dB. Thus, even with this smaller surface current, ranges exist at which large intensity differences occur. It is also important that at some ranges, intensity differences are small. Consequently, an experimenter using source-receiver pairs and attempting to sense current effects in part from intensity measurements in RT must necessarily take measurements at appropriate source-receiver ranges. Otherwise, current effects may not be expressed in intensity measurements.

Figure 10 illustrates a set of curves similar to those in Fig.9, but for a receiver depth of 75 m. At $\hat{r} = 5$ km and 9 km, relative intensity increases, and the net difference is about 3 dB over the interval of variation of $\hat{u}_{oo}$ from -1.0 to 1.0 ms^{-1}. At $\hat{r} = 6$ km and 10 km, intensity decreases by about 1 dB, while at 7 km the intensity decreases by 4 dB. For $\hat{r} = 8$ km, the intensity behaves differently, decreasing to a minimum at about $\hat{u}_{oo} = -0.1$ ms^{-1} and then increasing, with a net difference of about 4 dB over the interval. Thus, the behaviors of the relative intensity curves are completely different from those of Fig.9. For instance, the deep fade at 6 km in Fig.9 disappears from Fig.10, and the net difference at 10 km is

much smaller. The slope of each curve at 5, 7, and 9 km has changed sign, and the overall behavior of the 8 km curve has changed.

The results illustrated in Figs. 3 - 10 clearly show that the presence of currents can have a profound effect upon relative intensity. These numerical results are sufficiently intricate to make apparent that general predictions of the behavior of intensity with respect to any one parameter are generally impossible to make. Relative intensity appears to depend in a complex way upon current, source frequency, source depth, receiver depth, and source-receiver range. Concerning RT, our results indicate that source-receiver pairs may observe significant intensity differences over some range intervals, but could see only small intensity differences at other ranges. Thus, experimental data taken in RT may or may not include current-induced effects on intensity differences.

IV. SUMMARY

In this paper, we study effects of currents and current shear on underwater sound propagation using the parabolic equation method. To highlight current and current shear effects, we focus on the particular case in which boundary interfaces are horizontal, and both sound-speed and current are dependent on depth only. Also, we take the current to be horizontal and in the vertical source-receiver plane. The source emits a cw signal. We emphasize, however, that our procedures can be applied to more general problems, and this will be done in future work.

From basic fluid equations, a time-independent equation for the acoustic pressure field is derived. The standard assumptions of the parabolic approximation are applied to this governing equation. It is found that the approximate scaled equation contains three small parameters. These are:

e, measuring the maximum relative deviation of sound speed from a reference
value; Mach number M, the ratio of a reference current magnitude to a
reference sound speed; and ζ, measuring the maximum relative current shear.
It is essential to consider the relative sizes of these three parameters to
determine the appropriate parabolic approximation. In fact, a family of
parabolic equations is found, each of which is valid for different relative
magnitudes of these parameters. For some of these equations, we are able
to employ the notion of an effective sound-speed profile (ESSP), which is
actual sound speed modified by the addition of current. For these parabolic
equations, the ESSP allows incorporation of current effects in existing
numerical implementations of the parabolic equation. However, other members
of the family of parabolic equations would require new numerical
implementations.

We then present numerical computations for an isospeed channel of
100 m depth and with a lossy bottom. The cw source is at depth 25 m. The
current is taken to have a bilinear structure with surface current decaying
linearly to zero at mid-depth and remaining zero below this point. We
compute relative intensity as a function of range for surface currents
having different speeds and directions. The results, at different depths
and frequencies, show that there are range intervals with significant
intensity differences compared to the no-current case. There are also range
intervals that have small intensity differences. In addition, we consider
intensity as a function of depth and find that significant intensity differ-
ences tend to occur over large depth intervals as well. Finally, we show
intensity as a function of the surface current component, and results indicate
many different intensity-variation behaviors as the surface current changes.
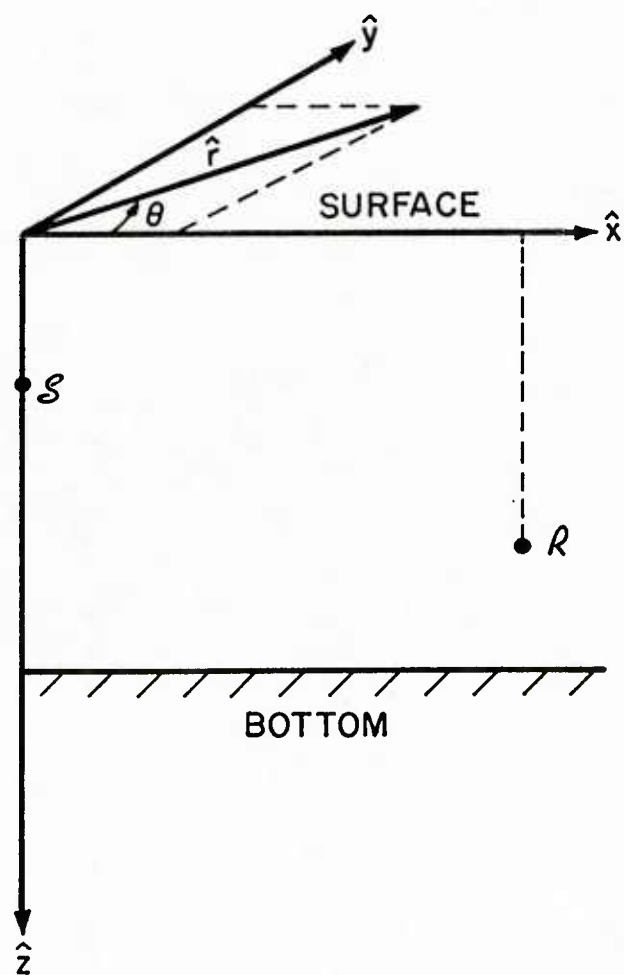When source and receiver are at the same depth, intensity differences in

reciprocal transmissions can be described from our results by reversing the sign of the current. We find that there are source-receiver separations at which large intensity differences exist, as well as those where there are small differences. We discuss implications of our numerical examples in the interpretation of experimental reciprocal data. In general, we find that variations in intensity with current profile for various frequency, source and receiver depth, and source-receiver range combinations are sufficiently complicated that there can be no simple characterization of current effects on intensity.

[1] R.P. Porter, "Acoustic Probing of Space-Time Scales in the Ocean," in Ocean Acoustics, ed. by J. DeSanto (Springer, New York 1978), pp.243-248.

[2] J.G. Clark and M. Kronengold, J. Acoust. Soc. Am., 56, 1071-1083 (1974).

[3] L. Nghiem-Phu and H.A. DeFerrari, J. Acoust. Soc. Am., 75, S25 (1984).

[4] L.A. Stallworth and M.J. Jacobson, J. Acoust. Soc. Am., 48, 382-391 (1970).

[5] L.A. Stallworth and M.J. Jacobson, J. Acoust. Soc. Am., 51, 1738-1750 (1972).

[6] L.A. Stallworth and M.J. Jacobson, J. Acoust. Soc. Am., 52, 344-355 (1974).

[7] E.M. Franchi and M.J. Jacobson, J. Acoust. Soc. Am., 52, 316-331 (1972).

[8] E.M. Franchi and M.J. Jacobson, J. Acoust. Soc. Am., 54, 1302-1311 (1973).

[9] J.A. Widtfeldt and M.J. Jacobson, J. Acoust. Soc. Am., 59, 852-860 (1976).

[10] R.F. Henrick, M.J. Jacobson, and W.L. Siegmann, J. Acoust. Soc. Am., 67, 121-134 (1980).

[11] P.F. Worcester, J. Acoust. Soc. Am., 62, 895-905 (1977).

[12] P.F. Worcester, J. Acoust. Soc. Am., 66, 1173-1181 (1979).

[13] W. Munk, B. Zetler, J. Clark, S. Gill, D. Porter, J. Spiesberger and R. Spindel, J. Geophys. Res., 86(C7), 6399-6410 (1981).

[14] P.M. Morse and K.U. Ingard, Theoretical Acoustics, (McGraw-Hill, New York 1968), pp.698-716.

[15] F.D. Tappert, "The Parabolic Approximation Method," in Wave Propagation in Underwater Acoustics, ed. by J. Keller and J. Papadakis (Springer, New York, 1977), pp.224-284.
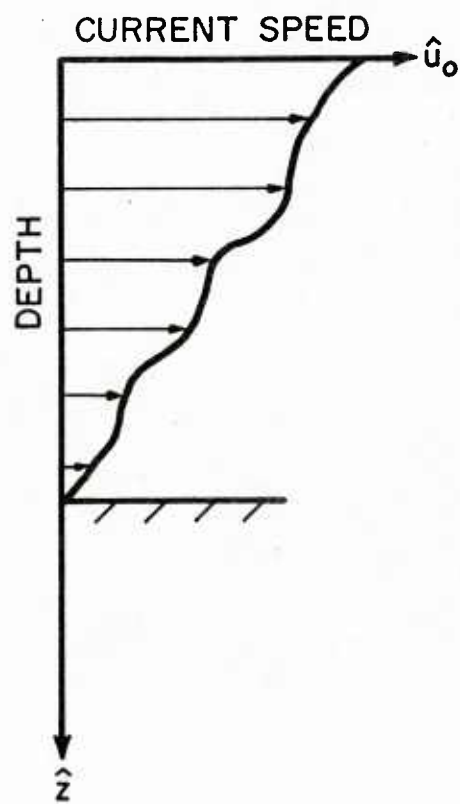
[16] M.K. Myers and G.L. McAninch, AIAA J., 16, 836-842 (1978).

[17] L. Nghiem-Phu and F. Tappert, "Reciprocity in the Time Domain and the Parabolic Equation Method," Rosenstiel School of Marine and Atmospheric Science, Univ. of Miami, Miami, FL (April 1984) (unpublished).

[18] S. Temkin, Elements of Acoustics (John Wiley, New York, 1981), p.34.

[19] G.A. Kriegsmann, D. Lee, and F. Tappert, "A Variable Density Parabolic Equation," in Recent Progress in the Development and Application of the Parabolic Equation, New London Lab., Nav. Underwater Sys. Ctr., New London, CT (May 1984), TD7145.

[20] M. Abramowitz and I. Stegun, Handbook of Mathematical Functions, (Dover, New York, 1965), p.364.

[21] T.B. Sanford, J. Acoust. Soc. Am., 56, 1118-1121 (1974).

[22] D. Lee and G. Botseas, "IFD: An Implicit Finite Difference Computer Model for Solving the Parabolic Equation," New London Lab., Nav. Underwater Syst. Ctr., New London, CT (May 1982), TR6659, AD-A117 701/3.

[23] F.B. Jensen and W.A. Kupermann, "Environmental Acoustic Modeling at SACLANTCEN," SACLANT ASW Research Ctr., La Spezia, Italy (1979), SR-34, AD-A081 853.
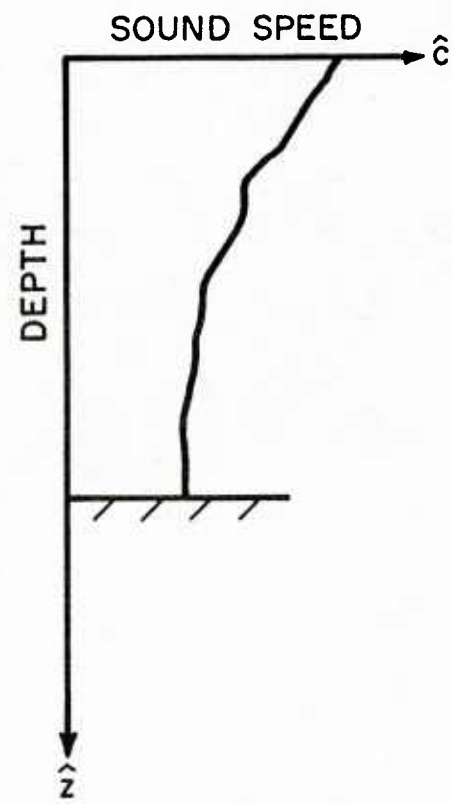
FIGURE LEGENDS

FIG.1.   (a) Horizontal ocean channel and coordinate systems, (b) general
current profile, (c) general sound-speed profile.

FIG.2.   Plane of Mach number M and maximum relative sound speed deviation ϵ,
showing significant terms in parabolic approximations.

FIG.3.   (a) Isospeed ocean channel, (b) current profile, (c) sound-
speed profile, (d) effective sound-speed profile.

FIG.4.   Relative intensity I versus range $\hat{r}$ for three current profiles;
$\hat{h}_S = 25$ m $= \hat{h}_R$, $\hat{h} = 100$ m, $\hat{c} = 1500$ ms^{-1}, $\hat{f} = 200$ Hz.

FIG.5.   Difference in relative intensity ΔI versus range $\hat{r}$, for three
current profiles. Parameters as in Fig.4.

FIG.6.   Relative intensity I versus range $\hat{r}$ for three current profiles; $\hat{h}_R = 100$ m,
other parameters as in Fig.4.

FIG.7.   Relative intensity I versus range $\hat{r}$ for three current profiles; $\hat{f} = 500$ Hz,
other parameters as in Fig.4.

FIG.8.   Relative intensity I versus receiver depth $\hat{h}_R$ for three current profiles;
(a) $\hat{r} = 7$ km, (b) $\hat{r} = 10$ km; other parameters as in Fig.4.

FIG.9.   Relative intensity I versus surface current speed $\hat{u}_{oo}$ for six
ranges; $\hat{h}_R = 25$ m, other parameters as in Fig.4.

FIG.10. Relative intensity versus surface current speed $\hat{u}_{oo}$ for six ranges;
$\hat{h}_R = 75$ m, other parameters as in Fig.4.

FIGURE 1

MAX. REL. SOUND-SPEED DEVIATION
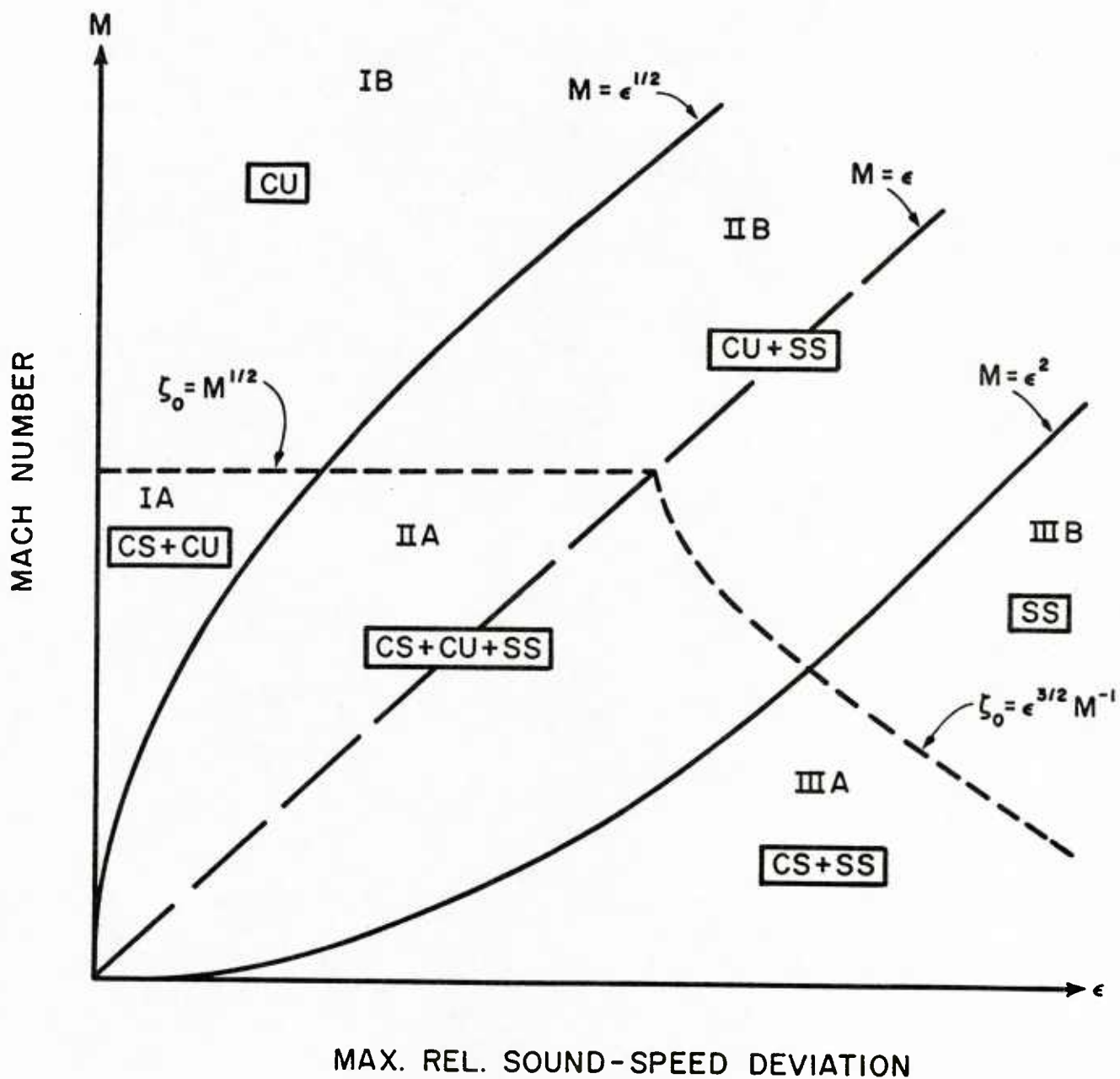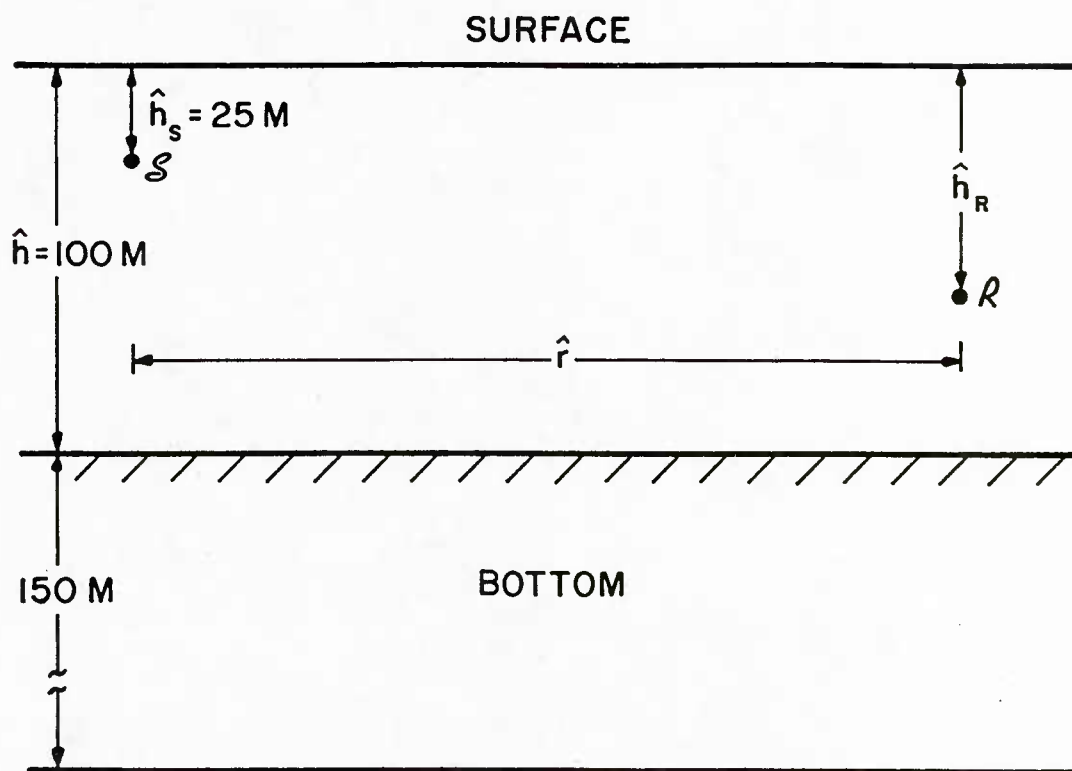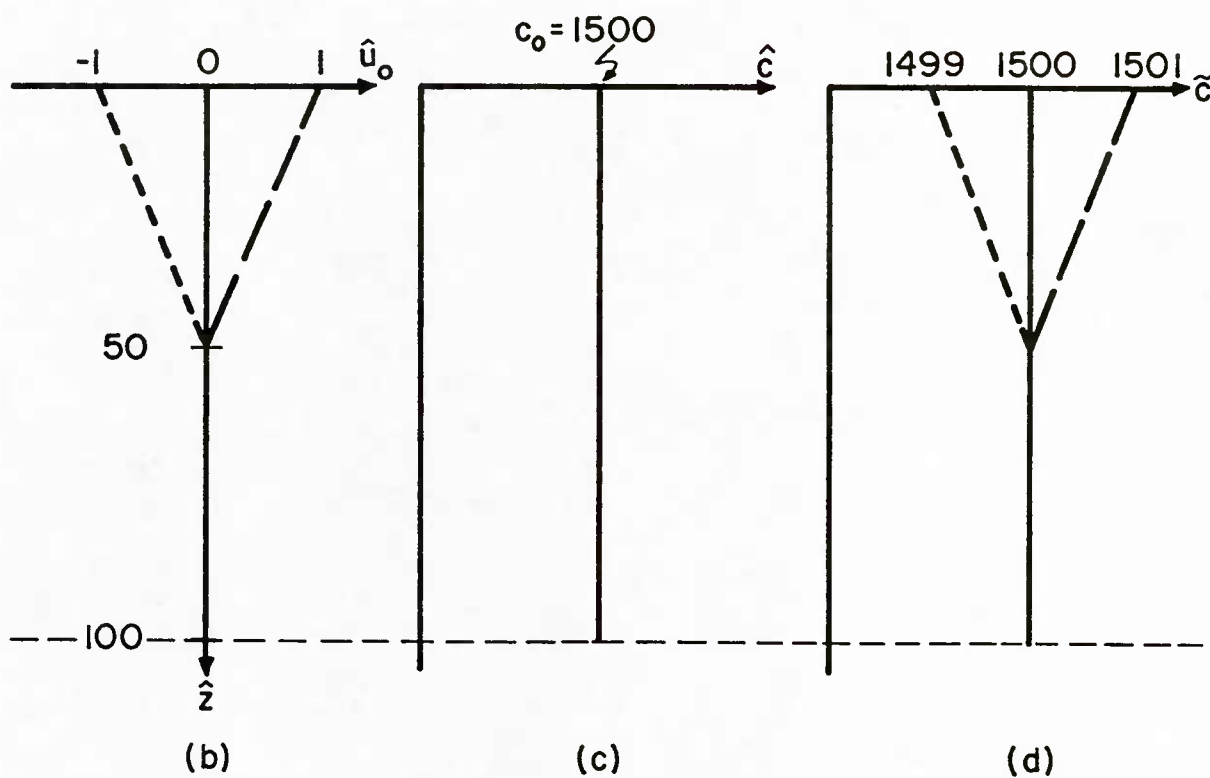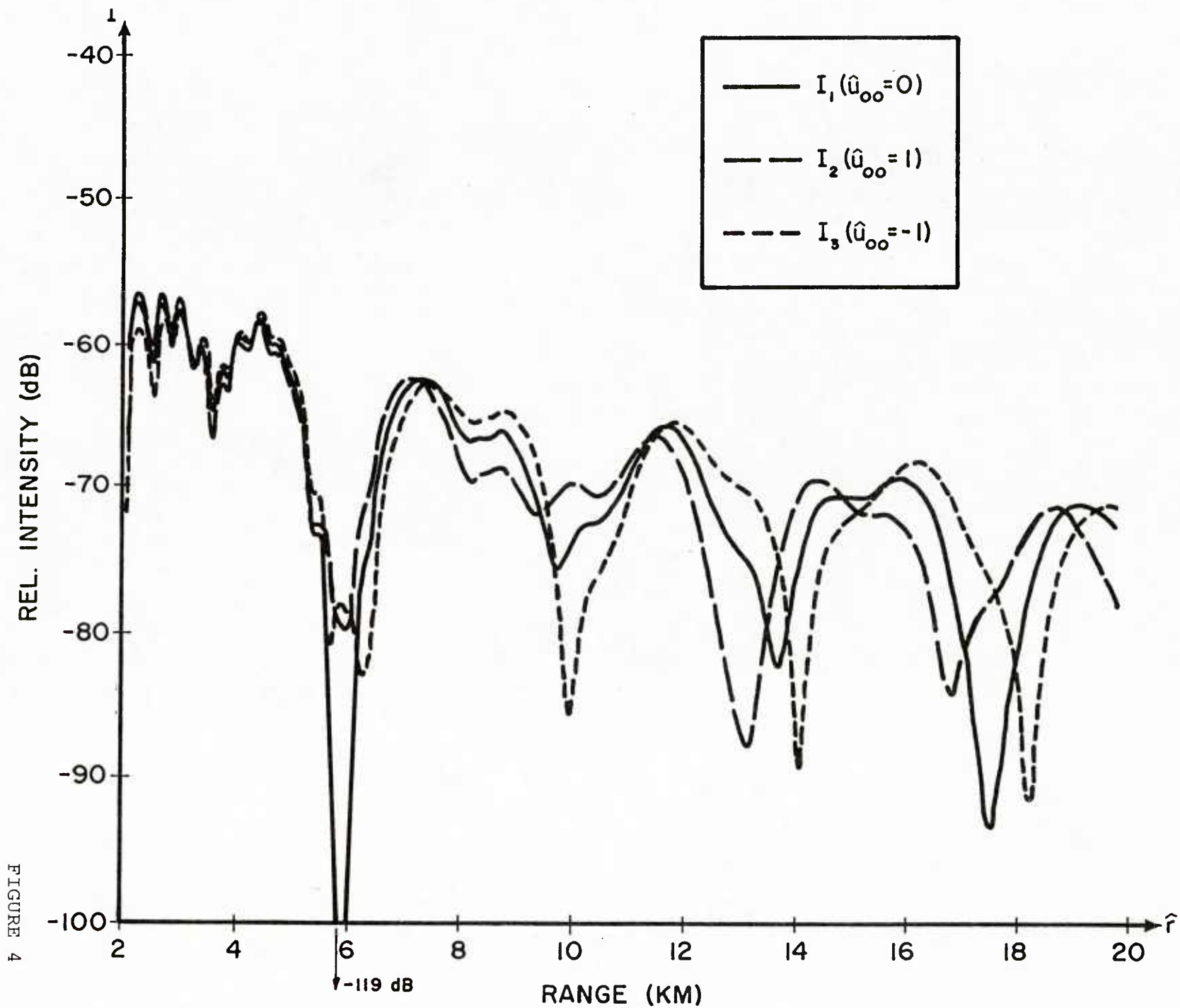
FIGURE 2

FIGURE 3

FIGURE 4

FIGURE 5

FIGURE 6

FIGURE 7

FIGURE 8

FIGURE 9

REL. INTENSITY (dB)

SURFACE CURRENT (MS^{-1})

$\hat{u}_{\infty}$

-119 dB

5 KM
6
7
8
9
10
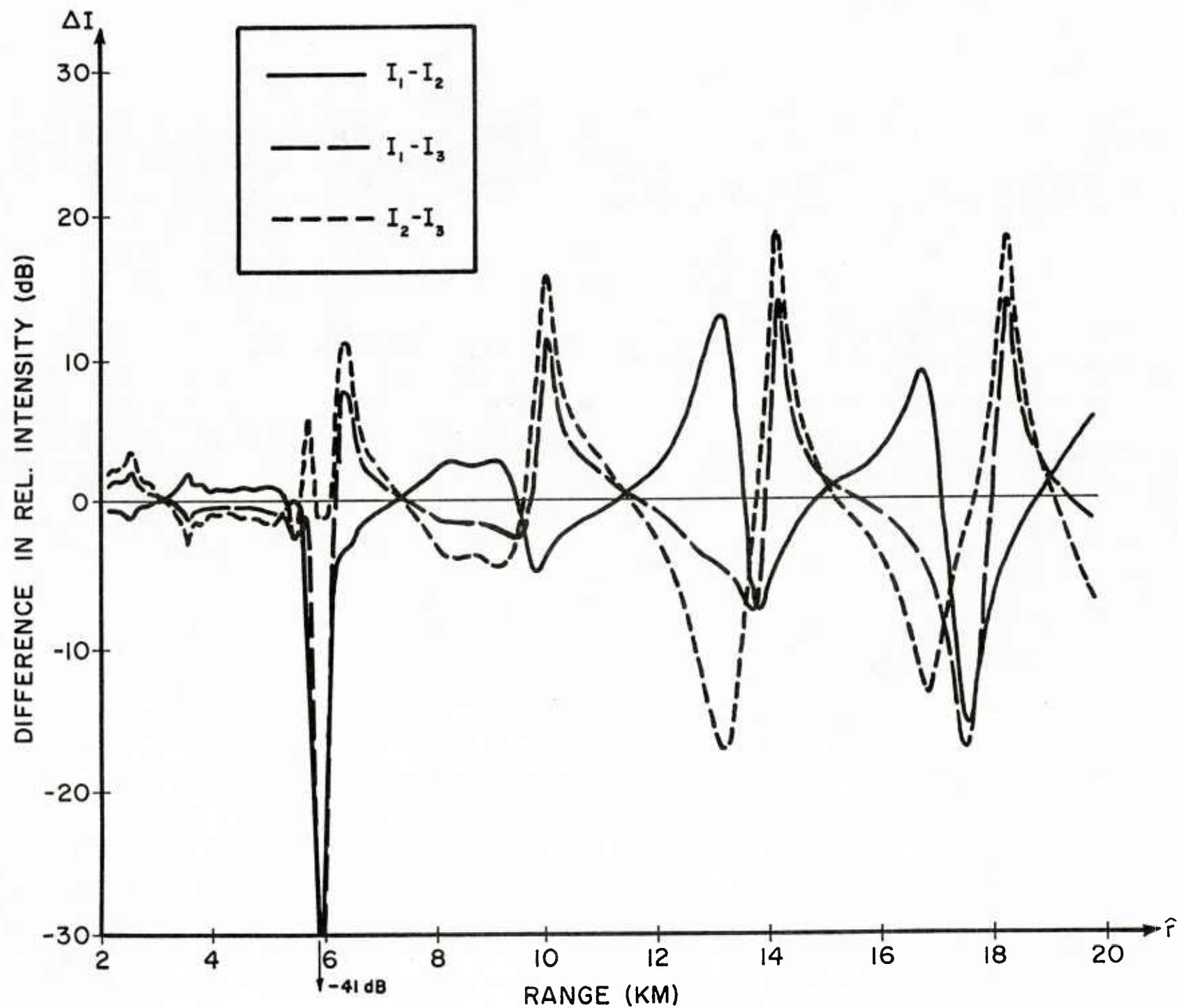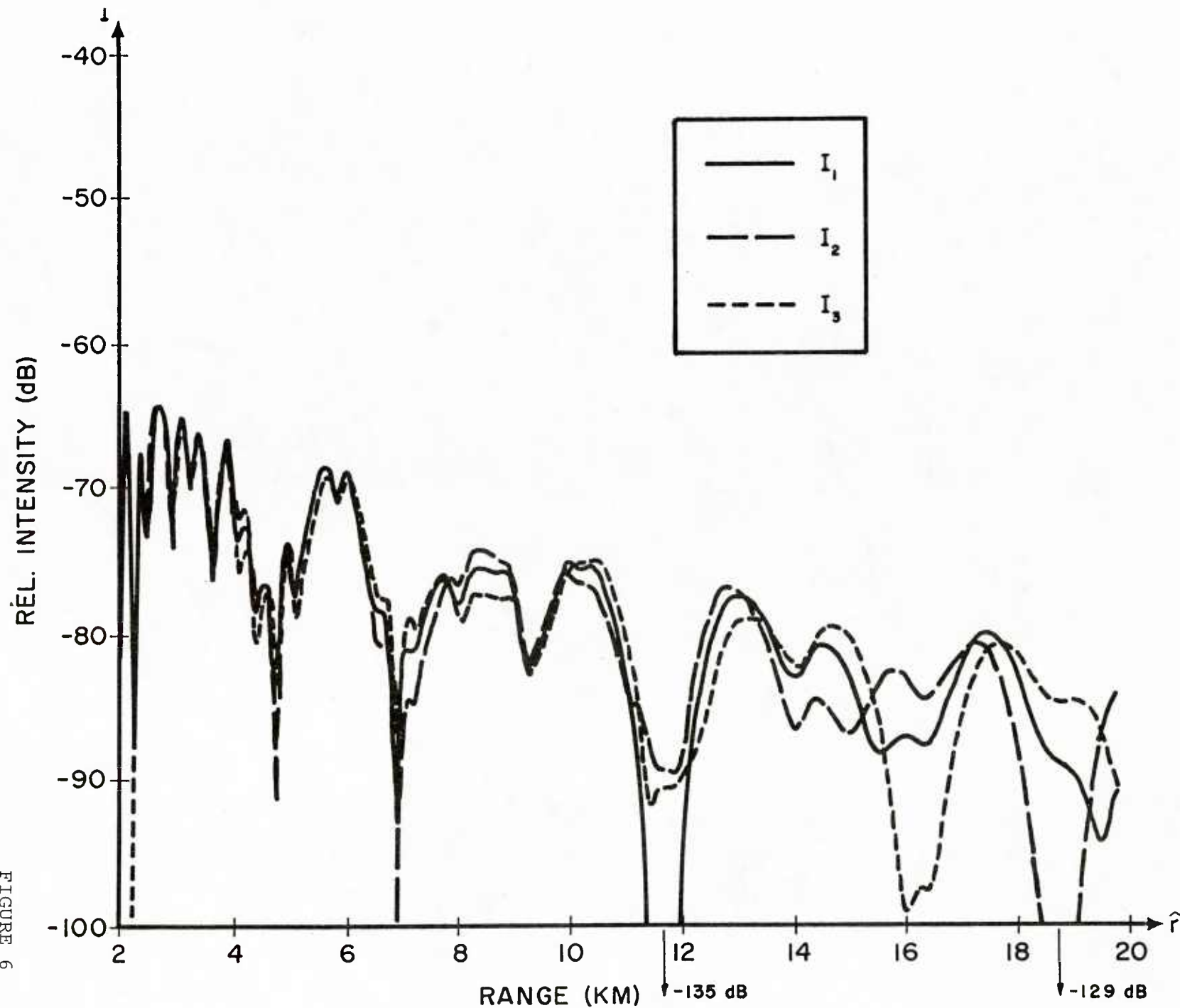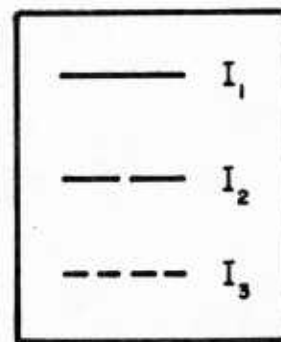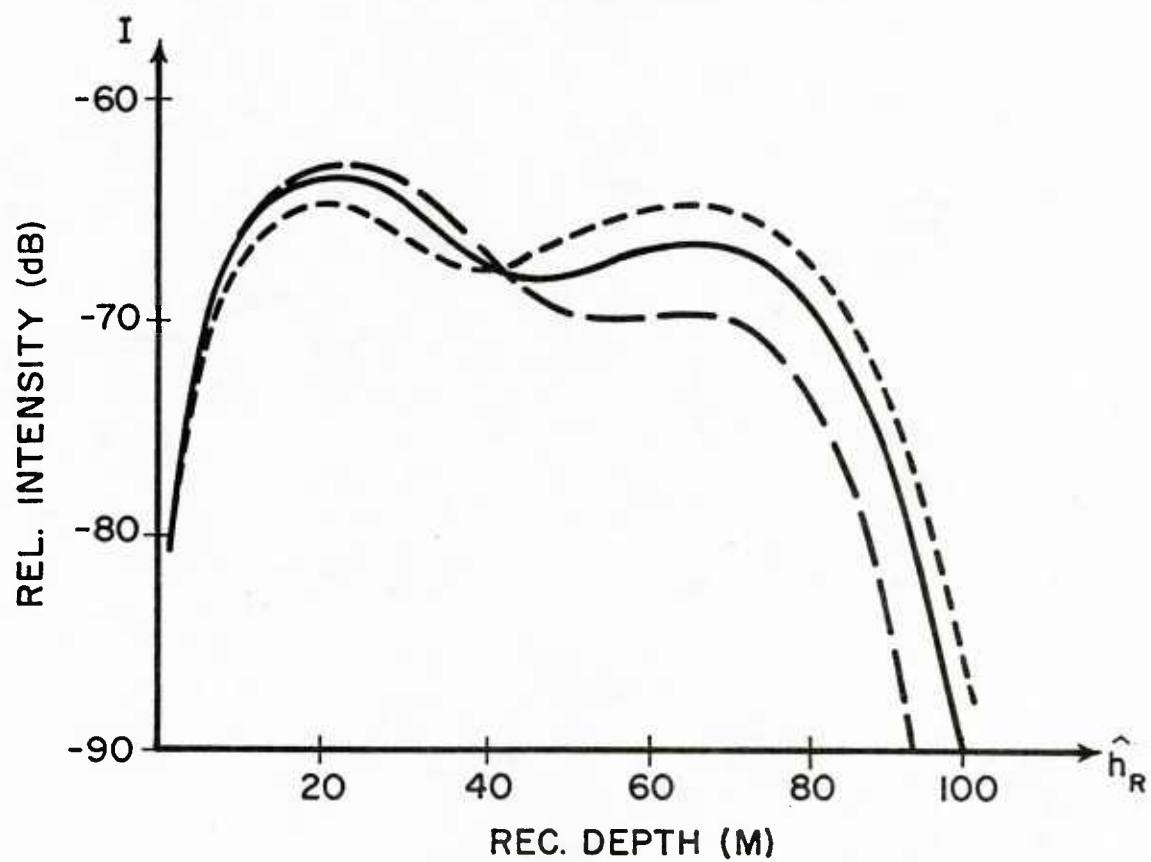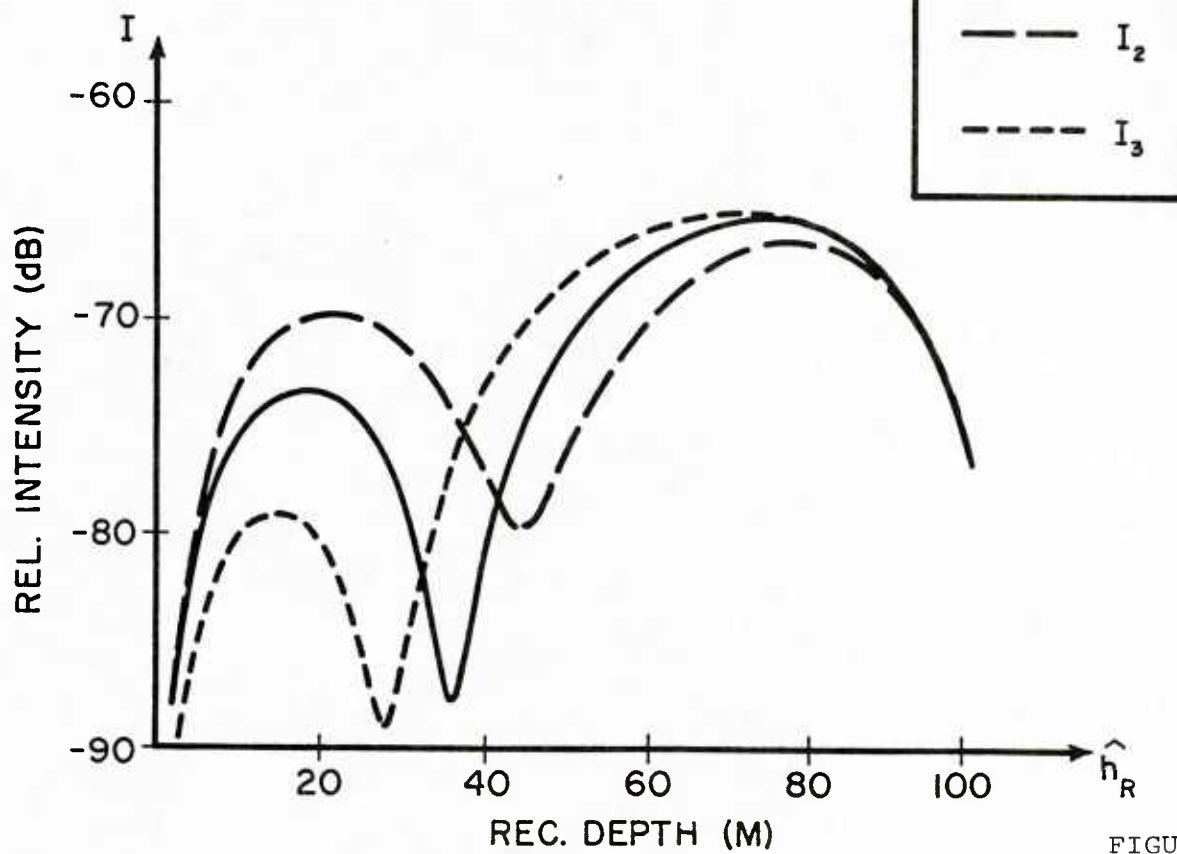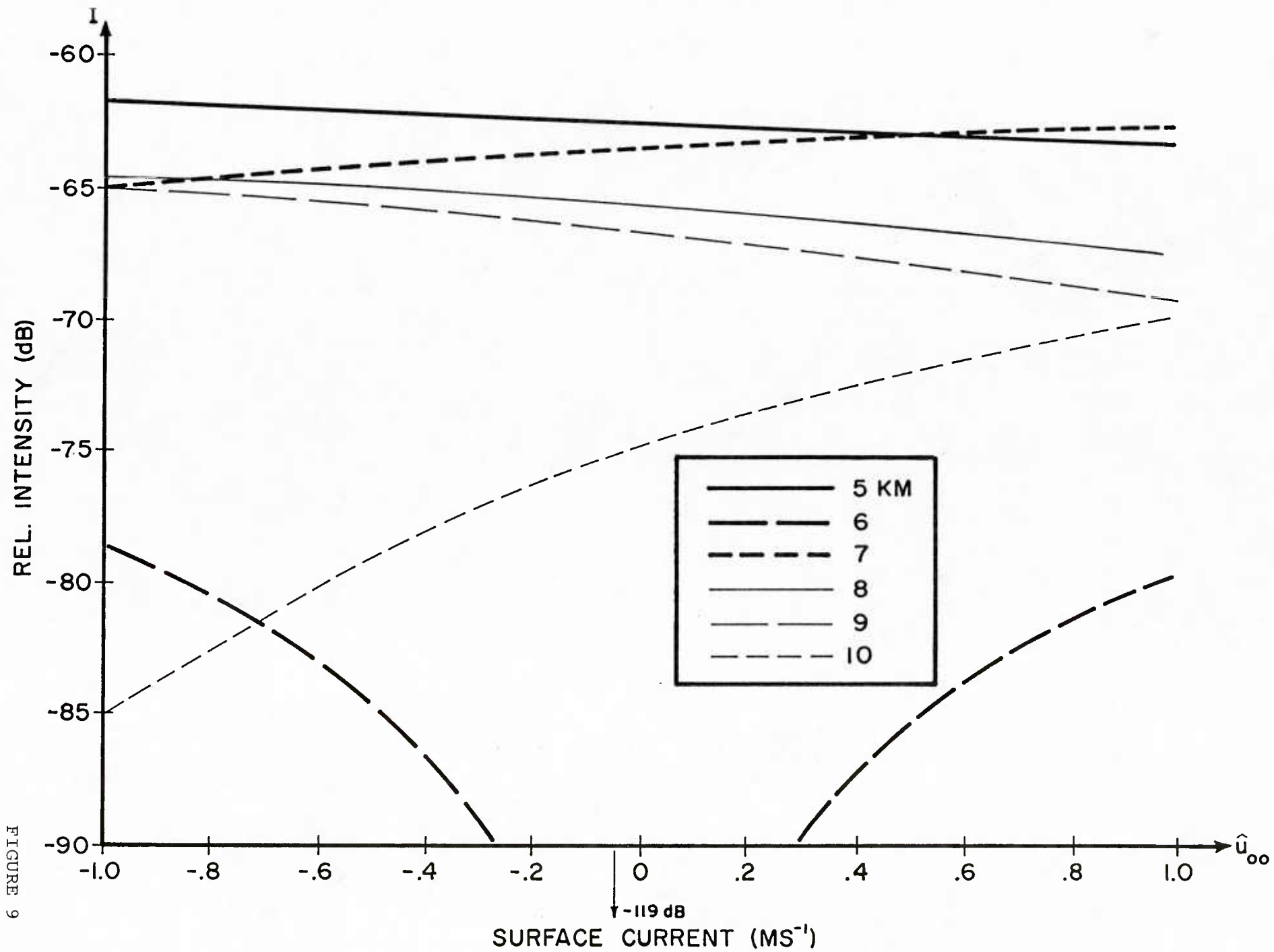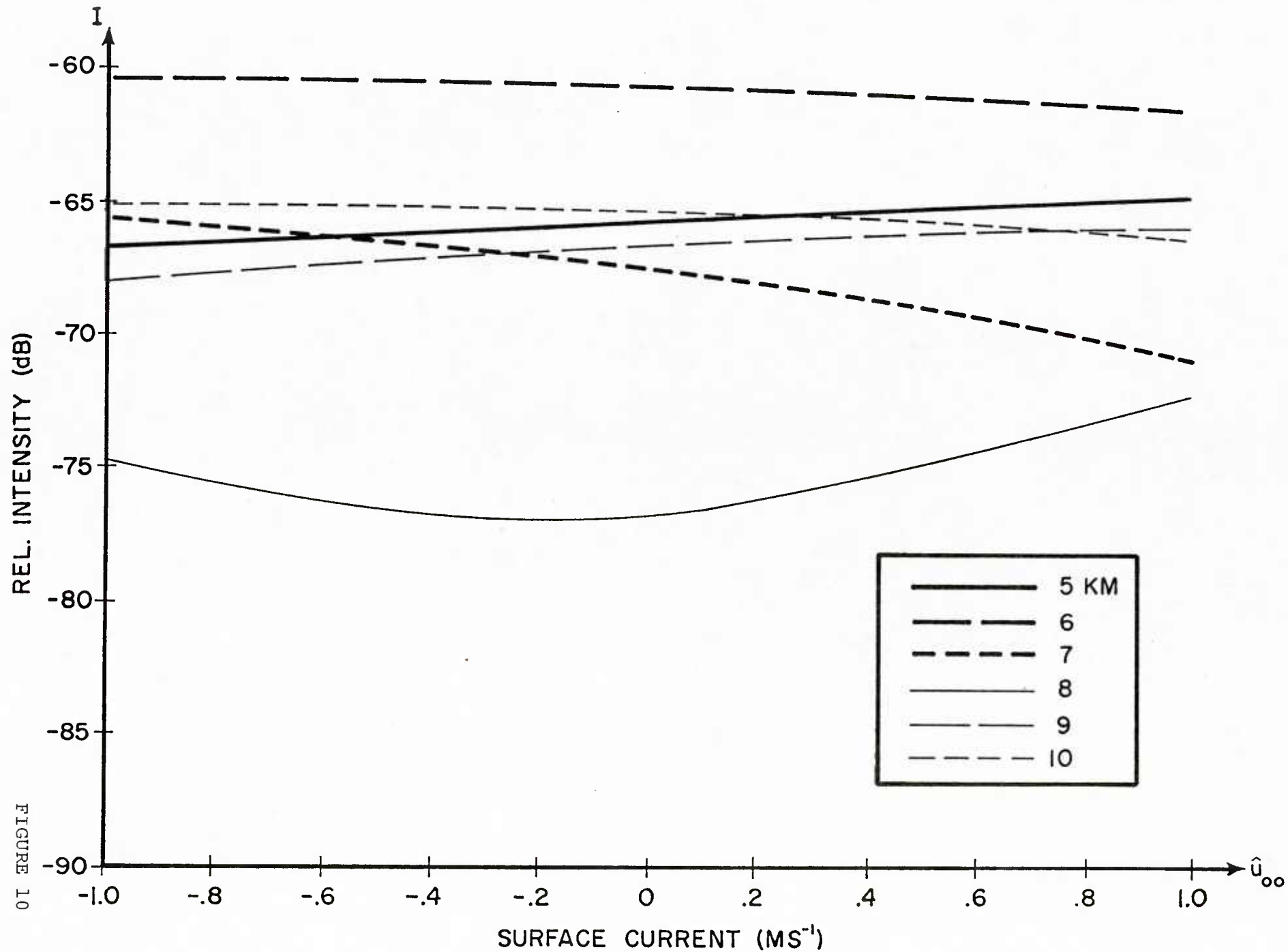
FIGURE 10

UNCLASSIFIED
DISTRIBUTION LIST
DEC 1981

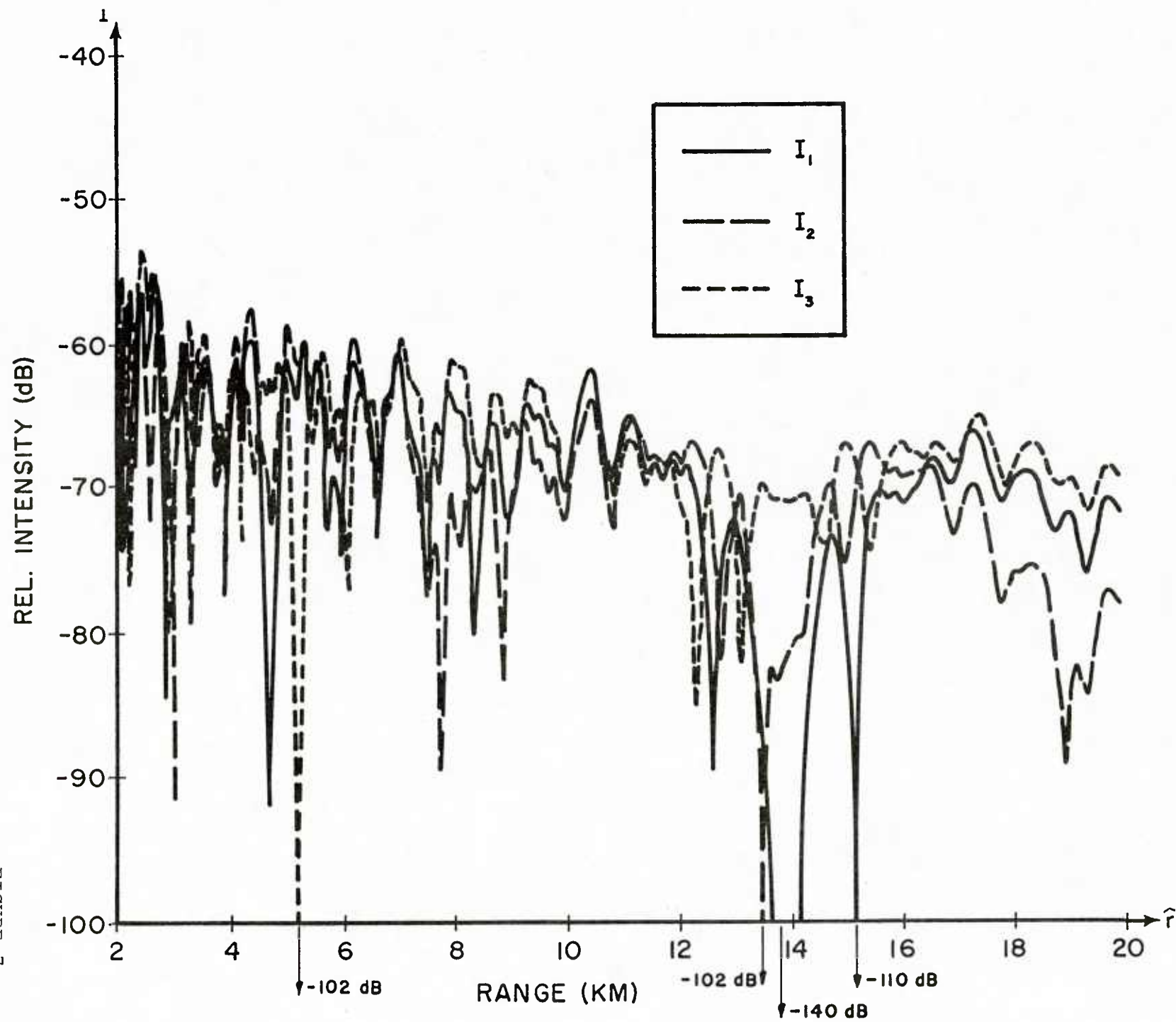| Addressee	No. of Copies	Addressee	No. of Copies
Office of Naval Research 800 North Quincy Street Arlington, Virginia 22217 Attn: Code 425AC 102 102C 210 220	2 1 1 1 1	Technical Director Naval Oceanographic Research and Development Activity NSTL Station Bay St. Louis, Mississippi 39522 Attn: Technical Director Dr. L. Solomon Dr. R. Gardner Mr. E. Chaika Mr. R. Van Wyckhouse Dr. S. W. Marshall	1 1 1 1 1 1
Office of Naval Technology 800 North Quincy Street Arlington, Virginia 22217 Attn: MAT 0721 MAT 0724	1 1	Director Naval Oceanographic Office NSTL Station Bay St. Louis, Mississippi 39522 Attn: Mr. H. Beck	1
Director Naval Research Laboratory 4555 Overlook Avenue, SW. Washington, D.C. 20375 Attn: Dr. J. C. Munson Mr. R. R. Rojas Dr. B. B. Adams Dr. W. B. Moseley Dr. J. P. Dugan Unclassified Library	1 1 1 1 1 1	Dr. T. M. Davis Mr. W. H. Geddes Dr. W. Jobst Mr. R. Merrifield Mr. R. A. Peloquin Dr. M. K. Shank	1 1 1 1 1 1
Superintendent Naval Research Laboratory Underwater Sound Reference Division P.O. Box 8337 Orlando, Florida 32806	1	Office of the Assistant Secretary of the Navy for Research, Engineering and Systems Washington, D.C. 20350 Attn: Dr. D. Barbe, Rm 4E732 Pentagon Dr. J. H. Probus, Rm 5E779 Pentagon	1 1
Director Office of Naval Research Branch Office 1030 East Green Street Pasadena, California 91106	1	Chief of Naval Operations Room 5D580, Pentagon Washington, D.C. 20350 Attn: OP951F	1
Office of Naval Research Rm 239, Campbell Hall University of California Berkeley, California 94720	1	Commander Naval Sea Systems Command Department of Navy Washington, D.C. 20362 Attn: Capt. James M. Van Metre PMS 409	1
Director Office of Naval Research Branch Office 495 Summer Street Boston, Massachusetts 02210	1	Chief of Naval Operations Office of the Director Naval Oceanographic Division OP-952	
Office of Naval Research New York Area Office 715 Broadway - 5th Floor New York, New York 10003	1	Department of the Navy Washington, D.C. 20352 Attn: Dr. R. W. James Capt. J. C. Harlett	1 1
Commanding Officer Office of Naval Research Branch Office Box 39 FPO New York 09510	1	Commander Oceanographic System, Atlantic Box 100 Norfolk, Virginia 23511	1
Director Office of Naval Research Branch Office 536 South Clark Street Chicago, Illinois 60605	1	Commander Oceanographic System, Pacific Box 1390 Pearl Harbor, Hawaii 96860	1
Office of Naval Research Resident Representative University District Building, Room 422 1107 North East 45th Street Seattle, Washington 98105	1		

Addressee	No. of Copies
Defense Advanced Research Projects Agency 1400 Wilson Boulevard Arlington, Virginia 22209 Attn: Capt. V. Simmons	1
ARPA Research Center Moffett Field Unit #1 California 94035 Attn: Mr. E. Smith	1
Commanding Officer Fleet Weather Central Box 113 Pearl Harbor, Hawaii 96860	1
Naval Ocean Systems Center (Kaneohe) Kaneohe, Hawaii 96863 Attn: Mr. D. Hightower Mr. B. Kishimoto Mr. R. Buecher	1 1 1
Commander Naval Electronic Systems Command 2511 Jefferson Davis Highway National Center #1 Arlington, Virginia 20360 Attn: CAPT C. A. Rose,, PME 124 LCDR P. Girard, NAVELEX 612	2
Commander Naval Air Systems Command Jefferson Plaza #1 1411 Jefferson Davis Highway Arlington, Virginia 20360	1
Commander Naval Sea Systems Command National Center #2 2521 Jefferson Davis Highway Arlington, Virginia 20362 Attn: SEA 63R 63Y	1 1
Commanding Officer Fleet Numerical Weather Central Monterey, California 93940 Attn: Mr. Paul Stevens Dr. D.R. McLain (NMFS)	1 1
Defense Documentation Center Cameron Station Alexandria, Virginia 22314	12
Commander Naval Ocean Systems Center Department of the Navy San Diego, California 92132 Attn: Dr. Daniel Andrews Dr. Dean Hanna Mr. Henry Aurand Dr. Harry A. Schenck	1 1 1 1

Addressee	No. of Copies
Commander Naval Surface Weapons Center Acoustics Division Silver Spring, Maryland 20910	1
Commander Naval Surface Weapons Center Science and Mathematics Research Group (K05) Dahlgren, Virginia 22448 Attn: Dr. E.W. Schwiderski	1
Commanding Officer Naval Underwater Systems Center New London Laboratory New London, Connecticut 06320 Attn: Dr. William Von Winkle Dr. A. Nuttall Mr. A. Ellinthorpe Dr. D.M. Viccione Mr. A. Donn Cobb	1 1 1 1 1
Commander Naval Air Development Center Department of the Navy Warminster, Pennsylvania 18974 Attn: Unclassified Library	1
Commanding Officer Naval Coastal Systems Laboratory Panama City, Florida 32401 Attn: Unclassified Library	1
Commanding Officer Naval Underwater Systems Center Newport Laboratory Newport, Rhode Island 02840 Attn: Unclassified Library	1
Commander David W. Taylor Naval Ship Research and Development Center Bethesda, Maryland 20084 Attn: Dr. M. Sevik	1
Superintendent Naval Postgraduate School Monterey, California 93940	1
Superintendent U.S. Naval Academy Annapolis, Maryland 21402 Attn: Library	1
Commanding Officer Naval Intelligence Support Center 4301 Suitland Road Washington, D.C. 20390 Attn: NISC 20	1
Director Applied Physics Laboratory University of Washington 1013 North East 40th Street Seattle, Washington 98105 Attn: Dr. T.E. Ewart Dr. M. Schulkin	1 1

Addressee	No. of Copies
Applied Research Laboratories University of Texas at Austin P.O. Box 8029 10000 FM Road 1325 Austin, Texas 78712 Attn: Dr. Loyd Hampton Dr. Charles Wood	1 1
Atlantic Oceanographic and Meteorological Laboratories 15 Rickenbacker Causeway Miami, Florida 33149 Attn: Dr. John Proni	1
Bell Telephone Laboratories 1 Whippany Road Whippany, New Jersey 07981 Attn: Dr. Bruce Bogart Dr. Peter Hirsch	1 1
Bolt, Beranek, and Newman, Inc. 50 Moulton Street Cambridge, Massachusetts 02238 Attn: Dr. K. L. Chandiramani	1
Chase, Inc. 14 Pinckney Street Boston, Massachusetts 02114 Attn: Dr. David Chase	1
Dr. David Middleton 127 East 91st Street New York, New York 10028	1
Duke University Department of Electrical Engineering Durham, North Carolina 27706 Attn: Dr. Loren Nolte	1
General Electric Company Heavy Military Electronic Systems Syracuse, New York 13201 Attn: Mr. Don Winfield	1
General Electric Company P.O. Box 1088 Schenectady, New York 12301 Attn: Dr. Thomas G. Kincaid	1
Gould, Incorporated Chesapeake Instrument Division 6711 Baymeadow Drive Glen Burnie, Maryland 21061 Attn: Dr. O. Lindemann	1
G R Associates, Inc. 10750 Columbia Pike Suite 602 Silver Spring, Maryland 20901 Attn: Dr. Sheldon Gardner Dr. Frank Rees	
Hughes Aircraft Company P.O. Box 3310 Fullerton, California 92634 Attn: Mr. S. W. Autrey	1

Addressee	No. of Copies
Hydroacoustics, Inc. 321 Northland Ave. P.O. Box 3818 Rochester, New York 14610	1
Institute for Acoustical Research Miami Division for the Palisades Geophysical Institute 615 South West 2nd Avenue Miami, Florida 33130 Attn: Mr. M. Kronengold Dr. J. Clark	1 1
Institute of Geophysics and Planetary Physics Scripps Institute of Oceanography University of California La Jolla, California 92093 Attn: Dr. W. Munk Mr. J. Spiesberger	1 1
Jaycor Incorporated 205 South Whiting Street Suite 607 Alexandria, Virginia 22304 Attn: Dr. S. Adams	1
Massachusetts Institute of Technology Acoustics and Vibration Laboratory 70 Massachusetts Avenue Room 5-222 Cambridge, Massachusetts 02139 Attn: Professor Patrick Leehey	1
Palisades Sofar Station Bermuda Division of Palisades Geophysical Institute FPO New York 09560 Attn: Mr. Carl Hartdegen	1
Polar Research Laboratory 123 Santa Barbara Avenue Santa Barbara, California 93101 Attn: Mr. Beaumont Buck	1
Research Triangle Institute Research Triangle Park Durham, North Carolina 27709 Attn: Dr. S. Huffman	1
Rensselaer Polytechnic Institute Troy, New York 12181 Attn: Dr. Melvin J. Jacobson	
Science Applications, Inc. 8400 Westpark Drive McLean, Virginia 22102 Attn: Dr. P. Tatro	
S.D.P. Inc. 15250 Ventura Boulevard Suite 518 Sherman Oaks, California 91403 Attn: Dr. M. A. Basin	1

Addressee	No. of Copies
Texas Instruments, Inc. 13500 North Central Expressway Dallas, Texas 75231 Attn: Mr. Charles Black	1
Underwater Systems, Inc. 8121 Georgia Avenue Silver Spring, Maryland 20910 Attn: Dr. M. Weinstein	1
University of Miami Rosenstiel School of Marine and Atmospheric Sciences 4600 Rickenbacker Causeway Miami, Florida 33149 Attn: Dr. H. DeFerrari	1
University of Michigan Department of Aerospace Engineering, North Campus Ann Arbor, Michigan 48109 Attn: Dr. W. W. Wilmarth	
University of Michigan Cooley Electronics Laboratory Ann Arbor, Michigan 48105 Attn: Dr. T. G. Birdsall	
University of Rhode Island Department of Electrical Engineering Wakefield, Rhode Island 02881 Attn: Dr. Donald Tufts	1
Woods Hole Oceanographic Institution Woods Hole, Massachusetts 02543 Attn: Dr. Paul McElroy Dr. R. Spindel	1 1